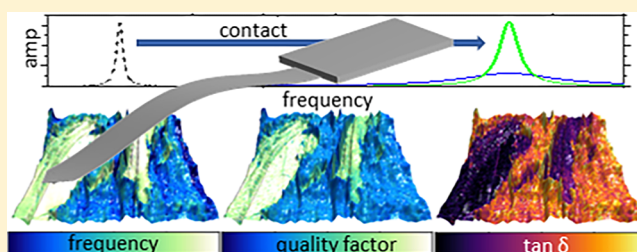


Contact Resonance Force Microscopy for Viscoelastic Property Measurements: From Fundamentals to State-of-the-Art Applications

Jason P. Killgore* and Frank W. DelRio*

Applied Chemicals and Materials Division, Material Measurement Laboratory, National Institute of Standards and Technology, Boulder, Colorado 80305, United States

ABSTRACT: Contact resonance force microscopy (CRFM) is an atomic force microscopy (AFM) method that evolved from a curiosity about the detection of ultrasonic vibrations with an AFM cantilever and an unaddressed need to characterize the mechanical properties of stiffer materials (elastic modulus >50 GPa). The method has matured to allow near-surface and subsurface elastic property measurements of single crystals, thin films, nanomaterials, composites, and other advanced materials. More recently, CRFM has been extended to viscoelastic property measurements, where the CR frequency and CR quality factor are utilized to quantitatively assess properties such as storage modulus, loss modulus, and loss tangent. In this Perspective, we trace the evolution of CRFM from initial discovery to elastic property measurements to viscoelastic property measurements. The techniques for extending single-point property measurements to two-dimensional property maps are then described in terms of their operational characteristics, demonstrated on calibration materials, and validated via comparisons to other viscoelastic measurement tools. The focus of the discussion then shifts to viscoelastic CRFM in nonambient conditions to highlight the challenges and developments related to thermomechanical analyses and liquid operation. The current state-of-the-art and best practices in data acquisition and analyses for viscoelastic CRFM are elucidated via a step-by-step demonstration on a wood–polymer composite. Finally, we conclude with a discussion of potential polymer science application areas that are poised to benefit from the recent advances in the ambient and nonambient CRFM methodologies. Altogether, we feel that the recent addition of CRFM to commercially available AFMs together with guides that clearly define state-of-the-art and best practices will accelerate its acceptance and adoption in polymer science via viscoelastic property measurements at unprecedented length and time scales.



INTRODUCTION

Polymeric materials are inherently viscoelastic, with mechanical properties that depend on time, frequency, and temperature.¹ With increasing control over the micro- and nanostructure of polymeric materials through copolymerization, blending, and nanocomposite filling, bulk characterization of viscoelastic behavior has become increasingly incomplete in its ability to inform processing–structure–property relationships in these advanced polymeric materials. To that end, local mechanical characterization techniques such as instrumented indentation^{2–4} and atomic force microscopy (AFM)^{5–7} have emerged to provide spatially resolved mechanical property information at ever smaller length scales. AFM in particular has sprouted numerous submethods of measuring the mechanical response of materials ranging from the pervasive force spectroscopy^{8–10} and its modern high-speed analogues^{11–14} to dynamic methods such as force modulation microscopy¹⁵ and multifrequency intermittent contact modes.^{16–18} While many of these techniques have achieved widespread acceptance and adoption, much of the use has been restricted to elastic property measurements. The polymer science community has struggled to find a nanoscale viscoelastic characterization technique that provides accurate and timely measurement of viscoelastic properties such as storage modulus, loss

modulus, and loss tangent and compares favorably and consistently with properties measured by bulk methods such as dynamic mechanical analysis and oscillatory rheometry. In both theory and application, contact resonance force microscopy (CRFM) has shown the requisite capabilities to achieve high-resolution characterization of viscoelastic materials. CRFM is a dynamic contact mode of AFM based on the determination of the resonance frequencies f_n and quality factors Q_n of an AFM cantilever in free space and in contact with a sample surface. The mechanical properties are inferred from the measured f_n and Q_n via analytical representations of the cantilever dynamics and tip–sample contact mechanics. CRFM has the following benefits over the more common AFM methods: (1) The linear tip–sample interaction is more straightforward to model than the nonlinear behavior in intermittent-contact modes. (2) The higher frequencies permit faster detection speeds to observe spatial and *in situ* changes. (3) The dynamic excitation allows for increased sensitivity via the amplification related to operating on resonance. (4) The accuracy and precision are significantly improved given its ties

Received: June 3, 2018

Revised: August 10, 2018

Published: September 6, 2018

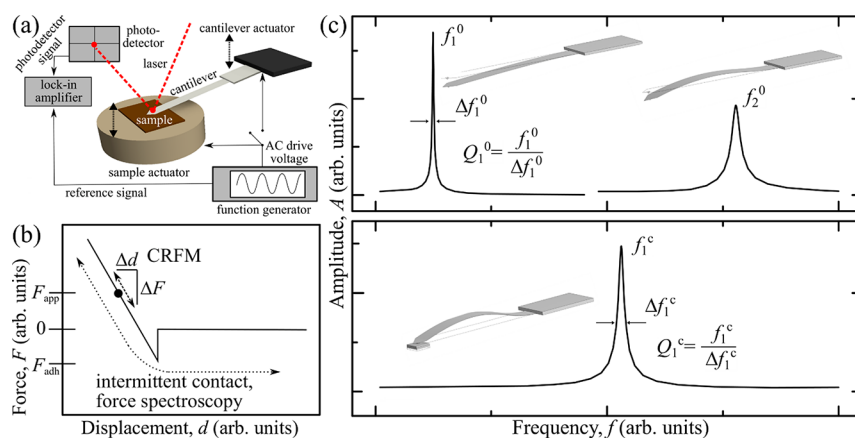


Figure 1. Schematic diagrams of (a) AFM setup, (b) force–displacement data, and (c) CRFM frequency spectra. In (a), dynamic excitation of the cantilever is achieved through piezoelectric actuation of the cantilever holder or sample surface. The motion of the cantilever is detected with the photodetector and compared to the reference signal via lock-in methods. In (b), the solid line represents the retract portion of a force–displacement trace, where F_{app} is the applied force and F_{adh} is the adhesion force. In intermittent-contact mode and force spectroscopy, the cantilever traverses much of the F – d trace, whereas in CRFM, the cantilever operates solely in the repulsive regime at small ΔF and $F_{app} \gg F_{adh}$ to ensure a linear tip–sample interaction. In (c), frequency spectra for a cantilever in free space (top) and in contact with a surface (bottom) are shown. In free space, the frequency response of the cantilever is defined in terms of the free resonance frequencies f_n^0 , full width at half maxima Δf_n^0 , and quality factors Q_n^0 . In contrast, the response of the cantilever in contact is defined in terms of the contact resonance frequencies f_n^c , full width at half-maxima Δf_n^c , and quality factors Q_n^c .

to frequency instead of displacement measurements. (5) The ability to operate on multiple cantilever eigenmodes enables the dynamic stiffness to be tuned to the material.

Historically, CRFM has been used to determine the elastic properties of *stiff* materials through piezoelectric excitation of the sample as in atomic force acoustic microscopy (AFAM)¹⁹ or the cantilever as in ultrasonic atomic force microscopy (UAFM).²⁰ In elastic CRFM, properties such as elastic modulus²¹ and Poisson's ratio²² are deduced solely based on changes to f_n from free space f_n^0 to contact f_n^c . Expectedly, a considerable amount of the method development was conducted on calibration materials like single-crystal Si, GaAs, InP, CaF₂, and MgF₂,^{23–25} as the well-defined structure–property relations enabled unbiased assessments of the experimental and analytical tools. Subsequent work then used the validated methods to explore the elastic properties of myriad advanced materials (i.e., new or modified materials designed to optimize properties for a specific application), using calibration materials as a reference to understand any unique properties. For example, several studies have explored the near-surface elastic properties of thin films and nanomaterials and reported values that differ from their bulk counterparts; the differences were attributed to chemical gradients, grain-size effects, and surface stresses and shown to vary with oxidation temperature, size, and processing.^{26–30} Other work has focused on subsurface elastic properties and behavior; in these studies, CRFM was used to detect subsurface dislocation formation and motion in highly oriented pyrolytic graphite,³¹ buried interfaces and voids in microelectronics,^{32,33} interfacial adhesion of a film–substrate system,³⁴ buried silica nanoparticles in a polymer matrix,^{35,36} and subsurface features in a polymer blend via three-dimensional tomographic reconstructions.³⁷ Finally, elastic CRFM has been used to study more complex phenomena such as *in situ* nanotribology³⁸ and heated-tip AFM^{39,40} and applications such as biofuel feedstocks,⁴¹ natural composites,⁴² and cellulose nanomaterials.⁴³

More recently, CRFM has been extended to study the viscoelastic properties of *soft* materials. In viscoelastic CRFM, storage modulus E' , loss modulus E'' , and loss tangent $\tan \delta$ are assessed by complementing knowledge of f_n with knowledge of the quality factor Q_n in free space Q_n^0 and in contact Q_n^c . More specifically, E' is strongly dictated by changes in f_n^c for most materials (i.e., low to moderate damping), whereas E'' and $\tan \delta$ are dependent on both f_n^c and Q_n^c for all materials.^{44–47} As such, quantitative viscoelastic CRFM is strongly dependent on the accurate determination of Q_n^c , as this facilitates a calculation of the sample quality factor Q_n^s after deconvoluting any environmental effects. However, accurate Q_n^c and thus Q_n^s measurements have proven problematic due to three main shortcomings: (1) cantilever actuation, (2) resonance acquisition and tracking, and (3) model design. On point 1, most early CRFM measurements employed acoustic excitation at either the sample or cantilever base, but these methods suffer from spurious vibrations, resulting in a “forest of peaks” in heavily damped materials and environments.^{48,49} Recent developments in magnetic,^{50,51} thermal,^{52,53} Brownian motion,⁵⁴ and electrostatic^{55,56} excitation schemes have largely addressed this issue via artifact-free responses in ambient and nonambient conditions. On point 2, most CRFM users require not only viscoelastic property measurements but also property maps, which required development of an understanding of the trade-offs between speed and accuracy for various tracking methods.^{57–65} Recent work has focused on these trade-offs as they pertain to viscoelastic CRFM.^{66,67} On point 3, early CRFM models omitted damping in the contact or failed to accurately account for damping in the environment. Now, beam models and hydrodynamic models have evolved to allow for accurate measurement of the damping phenomena.^{68–71} Given this progress, a considerable amount of method development has now been realized on calibration materials like polystyrene (PS), polypropylene (PP), and polyethylene (PE), thereby providing a basis for the end goal of work on advanced materials.

In this Perspective, we review and analyze the significant advances in CRFM for viscoelastic properties measurements in ambient and nonambient conditions to hopefully facilitate the jump from measurements on calibration materials to advanced materials. To this end, the fundamentals of viscoelastic CRFM are presented, with an emphasis on the experimental methods to obtain the frequency spectra of the cantilever in free space and in contact with the sample, followed by the analytical tools to assess the data in terms of the tip–sample interactions and ultimately the viscoelastic properties of the sample. The techniques for extending single-point property measurements to two-dimensional property maps are described in terms of their operational characteristics, demonstrated on calibration materials, and validated via comparisons to other viscoelastic measurement tools. The focus of the discussion then shifts to viscoelastic CRFM in nonambient conditions to highlight the challenges and developments associated with thermomechanical analyses and liquid operation, both of which are central to polymer design given the property dependence on temperature and environment. The current best practices in data acquisition and analyses for viscoelastic CRFM are then elucidated via a step-by-step demonstration on a wood–polymer composite with significant mechanical heterogeneity. Finally, we conclude with a discussion of some potential application areas that are poised to benefit from the recent advances in ambient and nonambient methodologies. At this juncture, it is important to note that this Perspective is not designed to provide a comprehensive review of the field, but instead to summarize and analyze seminal work and provide a framework for current best practices. More detailed descriptions of the experimental methods^{72,73} and analytical tools⁷⁴ can be found elsewhere. Furthermore, it is important to define the techniques that fall within our definition of CRFM. Here, we define CRFM as *on-resonance* continuous-contact methods that make use of small vibrations to induce *linear* tip–sample interactions (e.g., AFAM and UAFM); *subresonance* methods such as force modulation microscopy¹⁵ and *nonlinear* methods such as ultrasonic force microscopy⁷⁵ are beyond the scope of the Perspective.

■ FUNDAMENTALS

A schematic diagram of an AFM instrument is depicted in Figure 1a. Both imaging of a sample and measurement of mechanical properties are performed through interactions with a probe; the probe is at the end of a flexible cantilever that is attached to a holder controlled by the AFM instrument. As the probe is moved over the sample by either sample stage or cantilever holder motion, mechanical interactions between the probe and sample cause the cantilever to deflect. The deflection causes a laser beam that is reflected off the back of the cantilever to move over the surface of a photodiode detection system.⁷⁶ In an imaging mode such as contact mode⁷⁷ or intermittent-contact mode AFM,^{78–80} the probe is scanned parallel to the sample, and a feedback system coupled to the photodiode maintains the cantilever deflection or amplitude at a desired set point via the action of a piezoelectric actuator; the feedback signal is used to generate a topographic image. In force–displacement (F – d) spectroscopy,⁸¹ the feedback is turned off, the cantilever holder is moved perpendicular to the surface, and the deflection of the cantilever is measured as a function of the holder position. Appropriate calibration of the system enables the force F exerted by the sample on the probe to be determined as a

function of the cantilever displacement d , an example of which is shown in Figure 1b. Additional analyses of the F – d data enable mechanical properties of the sample to be determined; the probe can be moved to various locations on the sample to form “force–volume” maps of mechanical properties.

CRFM fundamentals are best described by comparing its operational characteristics to those of the more common AFM methods discussed above: contact mode, intermittent-contact mode, and force spectroscopy.^{72–74} Figure 1b illustrates the features of numerous modalities on the retract portion of the F – d trace. In intermittent-contact mode and force spectroscopy, the cantilever traverses much of the F – d trace, starting out of contact and then moving through both the attractive (adhesive) and repulsive (contact) regimes. In force spectroscopy, the loading profile is a low-frequency triangle wave, whereas intermittent-contact AFM is driven sinusoidally at or near the cantilever free resonance frequency f_1^0 . In contrast, contact mode AFM operates at a constant static force F_{app} with no modulation. CRFM relies on the feedback mechanism of contact mode, coupled with a modulation analogous to intermittent-contact mode. As shown in Figure 1c, the resonance frequency in contact f_1^c is shifted to a higher value compared to f_1^0 . The relative motion of the tip Δd and corresponding dynamic force on the surface ΔF are kept small compared to F_{app} to ensure that continuous contact is maintained and the motion is representative of the linear force gradient at the specified applied force.

Remarkably, developments in the field of CRFM largely progressed in the same order that a researcher might perform a CRFM experiment, with initial work focused on experimental methods to obtain frequency spectra, later work fixated on beam models to assess tip–sample stiffness and damping, and more recent work devoted to property measurements and mapping in both ambient and nonambient conditions. Clearly this is an oversimplification, given that much of the work occurred in parallel and iterative efforts, but provides a useful framework for the presentation of seminal CRFM papers.

Experimental Methods. Early work in CRFM focused on the development of metrologies to monitor ultrasonic vibrations of an AFM cantilever in the kilohertz to megahertz range and then characterize the resonant vibrational modes both out of contact and in contact with a sample surface (i.e., f_m^0 , f_w^c , Q_m^0 , and Q_w^c). Notably, two distinct groups made simultaneous, yet independent, progress on these metrologies. In 1994, Rabe and Arnold¹⁹ used sample excitation to induce cantilever vibrations well above the first free resonance frequency f_1^0 , with small sample vibrations in the linear portion of the F – d curve to simplify interpretation of the data. In this approach, a commercial AFM was modified to include an additional beam splitter, such that half of the laser beam from the cantilever was sent to an external knife-edge detector with a fast photodiode to track ultrasonic vibrations while the other half was sent to a traditional segmented photodiode to measure topography. The authors show clear correspondence between the topographic and amplitude signals, with feature resolution down to 100 nm in zoomed-in scans. In follow-up work, it was shown that $f_1^c > f_1^0$ and that there are local variations in f_1^c on different surfaces. The first point was credited to a change in the boundary condition of the cantilever, while the second point was attributed to variability in the elastic and chemical surface properties. Yamanaka and Nakano later demonstrated that CRFM was possible via ultrasonic vibration of the cantilever at its support, which eliminated the need for a

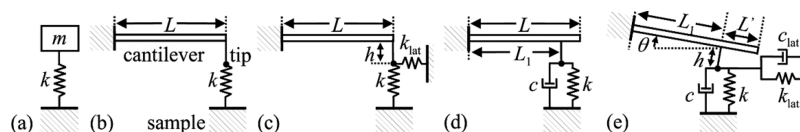


Figure 2. Point-mass and distributed-mass beam models used in CRFM. (a) In the point-mass model, the cantilever is replaced with a point-mass m attached to a surface via a spring of stiffness k . In the distributed-mass models, the cantilever is represented as a homogeneous beam of uniform cross section with a fixed end and a free (not shown) or surface-coupled (shown) end. The tip–sample interactions in the surface-coupled models are represented as a system of linear springs and dashpots. The common models include (b) k , (c) k and k_{lat} , (d) k and c , and (e) k , c , k_{lat} , and c_{lat} . In (d) and (e), the models also consider that the tip is offset from the fixed end of the beam by a distance L_1 .

transducer below the sample and the prospect of signal attenuation through the sample.²⁰ Another important point from this study relates to the higher eigenmode contact frequencies f_n^c and how they vary with normalized tip–sample contact stiffness $\alpha = k/k_L$, where k is the tip–sample contact stiffness and k_L is the cantilever stiffness. It was shown that f_n^c increases as α increases, but only over a limited range that varies with n . Consequently, f_n^c for $n = 1$ is useful for soft samples (small α), whereas f_n^c for $n > 1$ are more suitable for stiffer samples (large α). Finite element method (FEM) simulations were used to better explain this trend and concluded that the increase in α with n is due to the formation of nodes along the cantilever, which effectively reduces its length and enables stiffness evaluation of a wide range of materials.

Despite the advances in excitation schemes and ultrasonic detection, there were still numerous challenges related to the accurate determination of f_n^0 , f_n^c , Q_n^0 , and Q_n^c . Several of these issues were addressed through measurements and modeling of the frequency response and vibrational amplitudes of the cantilever in and out of contact with a surface; the frequency spectra enabled measurements of f_n^0 , f_n^c , Q_n^0 , and Q_n^c at several n , whereas the vibrational amplitudes provided quantitative insight into the appropriate models needed to describe the flexural vibrations. Rabe et al.⁸² examined both on four different cantilevers using optical interferometry and interpreted the results in terms of point-mass and distributed-mass beam models. In contact with a sample, the study showed good agreement between the two models for $k < k_L$ but also highlighted significant deviations in f_1^c/f_1^0 for $k > k_L$. An ensuing study showed that the two models also behave differently with respect to drive-point impedance (i.e., a ratio of system velocity to applied force or an estimate of accepted energy at a given f).⁸³ These differences are especially important when the excitation frequency is above the resonance frequency of the first flexural mode ($f > f_1^0$). As such, it was suggested that caution should be exercised when using point-mass models (see Figure 2a) in CRFM, a major motivator for the focus on distributed-mass beam models as described later in this section. A second key finding by Rabe et al.⁸² was related to cantilever and tip–sample damping; the authors keenly noted that fluctuations in Q_n^0 are likely due to changes in sound radiation and friction with air, whereas variations in Q_n^c are due to changes in sample damping. These conclusions about Q_n^0 and Q_n^c form the basis for viscoelastic CRFM. Yamanaka et al.⁸⁴ later showed that the vibrational spectra were also strongly dependent on the excitation power of the actuation transducer. It was observed that both f_n^c and Q_n^c decreased as excitation power increased. The general trend was described in terms of changes to the tip–sample interaction. At small excitation powers, k can be regarded as constant during an actuation cycle, resulting in a linear tip–sample contact and a single peak

in the frequency spectrum. In contrast, k can vary in a single actuation cycle at larger powers, leading to nonlinear behavior and spectra with broader peaks at smaller frequencies (these nonlinear peaks are the sum of linear spectra for different k). The proposed solution to this issue was to operate at small excitation powers, where f_n^c and Q_n^c converged to their infinitesimally small amplitude condition.

Model Development. Given the improvements in the metrology and interpretation of f_n^0 , f_n^c , Q_n^0 , and Q_n^c , subsequent efforts focused on analytical and FEM models to describe the dynamics of the cantilever in free space and in contact with a surface. As noted earlier, it has been demonstrated that point-mass beam models as shown in Figure 2a are only valid for $k < k_L$ and $f \approx f_n^0$ making them invalid on most practical CRFM samples. Consequently, most work focused on the development of distributed-mass models, using Euler–Bernoulli beam theory as the framework. In free space, the cantilever dynamics are well-described by a distributed-mass fixed-free model,⁸² with the cantilever damping defined as $\chi = 2\pi f_n^0/Q_n^0$. However, when the tip is in contact with a sample, the cantilever model must be modified to include the effects of the tip–sample interactions. Here, it is typically assumed that the vibrational amplitudes are so small that the interactions at the tip can be represented as a system of linear springs and dashpots. Yamanaka and Nakano²⁰ and Rabe et al.⁸² considered the simplest case of a normal spring of stiffness k at the end of the cantilever of length L as shown in Figure 2b. The characteristic equation for a fixed-spring-coupled beam is a combination of the fixed-free and fixed-pinned equations, such that it transitions to the former for $k = 0$ and the latter for $k \rightarrow \infty$.⁷⁴ As shown in Figure 2c, Wright and Nishiguchi⁸⁵ extended the characteristic equation to include the effects of a lateral spring of stiffness k_{lat} and the tip height h . On inspection of the equation, the relative significance of k_{lat} and k on the cantilever shape and its dependence on k/k_L becomes apparent. For small k/k_L , the effect of k_{lat} on the cantilever shape is small, given its weight is dependent on h^2/L^2 (h^2/L^2 ranges from 0.15 to 0.0125 for common CRFM cantilevers).⁷⁴ In contrast, k_{lat} has a significant impact on the shape at large k/k_L and small n , suggesting that it can no longer be neglected.⁸⁶ This becomes an important consideration in the best practices section later.

The models described above permitted CRFM elastic property measurements but still missed some of the necessary elements to conduct quantitative viscoelastic CRFM property measurements. Rabe et al.⁶⁸ addressed one of the shortcomings through the inclusion of a dashpot with damping c in parallel with a normal spring of stiffness k in the characteristic equation; this spring–dashpot pair is often termed a Kelvin–Voigt element and, in this case, was placed at the end of the cantilever. Rabe et al.²¹ later considered the characteristic equation for a fixed-spring-coupled beam, where the tip is offset from the fixed end of the beam by a distance L_1 (or

conversely, offset from the free end by a distance $L' = L - L_1$). The new equation showed that L' has a significant impact on the extracted value of k/k_L and that the magnitude of this effect is dependent on n , which highlighted that its inclusion in successive models was a requisite for accurate CRFM viscoelastic measurements. Hurley and Turner⁶⁹ combined the two features to arrive at the characteristic equation for a beam with both damping and tip position effects, an example of which is shown schematically in Figure 2d. For convenience, c is normalized by the cantilever properties to $\beta = cL_1/(9E_L I \rho A)^{1/2}$, where E_L , I , ρ , and A are the elastic modulus, moment of inertia, density, and cross-sectional area, respectively. In this configuration, the cantilever dynamics are defined by a complex normalized wavenumber $\lambda_n L = a_n + ib_n$, where $a_n = x_n^0(f_n^c/f_n^0)^{1/2}$ is the real part of $\lambda_n L$ and $b_n = a_n[(2\pi f_n^c - \chi Q_n^c)/8\pi f_n^c Q_n^c]$ is the imaginary part of $\lambda_n L$. The values for $x_n^0 L$ are the solutions to the characteristic equation for free flexural resonance as defined by $1 + (\cos x_n^0 L) \cosh x_n^0 L = 0$. As such, $x_n^0 L = \{1.8751, 4.6941, 7.8548, 10.996\}$ for $n = 1-4$. From the calculated $\lambda_n L$, α and β are found from the real and imaginary parts of

$$\alpha + i\beta(\lambda_n L_1)^2 = \frac{2}{3}(\lambda_n L_1)^3 \frac{[1 + \cos \lambda_n L \cosh \lambda_n L]}{D} \quad (1)$$

where

$$\begin{aligned} D = & ((\sinh \lambda_n L_1 \cos \lambda_n L_1 - \sin \lambda_n L_1 \cosh \lambda_n L_1) \\ & \times (1 + \cos \lambda_n L' \cosh \lambda_n L')) \\ & + ((1 - \cos \lambda_n L_1 \cosh \lambda_n L_1)(\sin \lambda_n L' \cosh \lambda_n L' \\ & - \cos \lambda_n L' \sinh \lambda_n L')) \end{aligned} \quad (2)$$

L_1 and L' are most often determined via a “mode-crossing” approach,²¹ which involves plotting α as a function of relative tip position $\gamma = L_1/L$ for two flexural modes and then taking the value of γ from the point at which the two curves intersect. However, it is important to note that γ calculated in this way is an effective tip position, which varies depending on the two modes utilized in the approach and is often different than the offset measured via optical or electron microscopy, most likely due to deviations in the real cantilever properties from those in the idealized Euler–Bernoulli model.^{22,87} In most cases, this model is adequate for CRFM viscoelastic property measurements, given that it includes most of the relevant elements while also minimizing the number of unknown or difficult-to-measure parameters. As a result, it has been used in several of the following studies and is also highlighted in the best practices section. In select cases, however, additional layers of complexity are required to better capture the experimental details. The model developed by Dupas et al.⁸⁸ shown in Figure 2e captures many of these additional elements through the addition of a lateral Kelvin–Voigt component (to include lateral stiffness and damping) and cantilever tilt (which is $\approx 10^\circ$ – 15° for most commercially available AFMs). Some conditions where this model might be more appropriate will also be discussed in the best practices section.

■ VISCOELASTIC PROPERTY MEASUREMENTS

The seminal papers described above provided the foundation for viscoelastic property measurements via CRFM. More specifically, the work provided the experimental methods to obtain the frequency spectra for the cantilever in and out of

contact (i.e., f_n^0 , f_n^c , Q_n^0 , and Q_n^c) and the analytical tools to convert these measured values into the normalized tip–sample stiffness and damping (e.g., α and β). Several studies have subsequently reported on methods to convert α and β to viscoelastic properties such as E' , E'' , and $\tan \delta$. The explicit determination of E' and E'' has proven difficult given their dependence on contact area of the AFM probe, but this problem has largely been obviated through a comparative approach. In contrast, $\tan \delta$ does not require an intermediate calculation of E' and E'' , thereby negating the need for calibration measurements. It is important to note that both methods (like all AFM-based nanomechanics methods) are vulnerable to uncertainties in tip geometry, contact area, and material nonlinearity in the tip–sample contact arising from high contact pressures. Dokukin and Sokolov illuminated this point through a systematic study of three polymers with three AFM probes of well-defined geometry.⁸⁹ The authors ultimately verified that artifact-free data can be obtained by utilizing larger radius tips (e.g., 810 and 1030 nm) and including adhesive effects in the models, which minimize nonlinearity in the stress–strain relation and lead to more accurate depictions of the contact area. For CRFM, the fact that measurements are often obtained through a comparative approach helps to hide these issues but should be recognized in cases where absolute quantification is required.

Storage and Loss Modulus. Yuya et al.⁴⁴ developed an approach to convert the measured values for α and β into E' and E'' . To measure α and β , the amplitude and phase response of the cantilever were measured in and out of contact with the sample, and the spectra were fit to the theoretical response for a cantilever subjected to harmonic excitation. α and β were used to calculate E' and E'' via a contact mechanics model of the tip–sample interaction. The contact model used in the paper is based on Hertzian mechanics,⁹⁰ which describes the contact between a sphere of radius R and a flat surface. Under an applied load F , the sphere and flat surface form a contact over a circle of radius $a_c = (3FR/4E^{*R})^{1/3}$, where E^{*R} is the reduced complex modulus. For a linear viscoelastic material

$$E^{*R} = E'^R + iE''^R = \frac{k}{2a_c} + i\frac{\pi f_n^c c}{a_c} \quad (3)$$

where E'^R is the reduced storage modulus and E''^R is the reduced loss modulus. Consequently, with an accurate measurement of a_c , it is possible to calculate both E'^R and E''^R . However, it is extremely difficult to independently measure the contact radius, as values for a_c are typically on the order of a nanometer. To circumvent this issue, a comparative approach has been developed, where alternating measurements on the sample of interest and a sample with predetermined storage E'_{cal} and loss E''_{cal} moduli are taken.^{44,87,91} In this approach, the values for E'_{cal} and E''_{cal} are first used to calculate calibration values for the normalized contact stiffness α_{cal} and damping β_{cal} via eqs 1 and 2 and then used to calculate the reduced storage E'_{cal}^R and loss moduli E''_{cal}^R per

$$E'_{\text{cal}}^R + iE''_{\text{cal}}^R = \left[\frac{1 - \nu^2}{E'_{\text{cal}} + iE''_{\text{cal}}} + \frac{1 - \nu_{\text{tip}}^2}{E_{\text{tip}}} \right]^{-1} \quad (4)$$

Equation 4 assumes identical Poisson's ratios ν for the unknown and calibration materials and knowledge of the elastic modulus E_{tip} and Poisson's ratio ν_{tip} of the tip. With α_{cal}

β_{cal} , $E_{\text{cal}}^{\text{R}}$, and $E_{\text{cal}}^{\text{NR}}$, E^{R} and E^{NR} are found via $E^{\text{R}} = E_{\text{cal}}^{\text{R}}(\alpha/\alpha_{\text{cal}})^{3/2}$ and $E^{\text{NR}} = E_{\text{cal}}^{\text{NR}}(f_n^{\text{c}}\beta/f_{n-\text{cal}}^{\text{c}}\beta_{\text{cal}})^{3/2}$, respectively. Finally, E' and E'' are assessed from E^{R} and E^{NR} with an expression similar to eq 4. In all, this analysis is based on small damping (i.e., $a_n \gg b_n$) and negligible tip damping and is therefore most applicable when measuring polymers in their solid state (e.g., well below the transition temperature) with silicon or silicon nitride tips. The authors validated the approach using poly(methyl methacrylate) (PMMA) as the test sample and PS as the calibration sample; $E_{\text{cal}}^{\text{R}}$ and $E_{\text{cal}}^{\text{NR}}$ for the PS sample were 5.1 ± 0.1 GPa and 117 ± 35 MPa, respectively, as measured by instrumented indentation. To simplify further discussion, the authors reported their findings based on storage $M' = E'/(1 - \nu^2)$ and loss $M'' = E''/(1 - \nu^2)$ indentation moduli. Using the approach outlined above, M' and M'' for the PMMA sample were determined for both $n = 1$ and $n = 2$. The reported values for M' and M'' exhibited slight variations with n , which was attributed to the cantilever shape, the cantilever clamping conditions, and conical tip mass effects. For all n , the average values for M' and M'' were found to be 8.1 ± 0.9 GPa and 190 ± 30 MPa, respectively, which are in agreement with previous measurements on PMMA.^{92–94} The differences between CRFM and previously reported results were attributed to an increase in transition temperature with load and nonlinear elastic effects at the tip–sample contact.⁹⁵

In later work,⁴⁵ the same authors extended their approach to study the relationship between β and Q_n^{c} , thereby obviating the need for phase spectra to determine E'' . From the analysis, the measured value of Q_n^{c} was defined as

$$(Q_n^{\text{c}})^{-1} = (Q_n^{\text{o}})^{-1} + (Q_n^{\text{s}})^{-1} \quad (5)$$

where $(Q_n^{\text{s}})^{-1} = 4b_n/a_n$ is the sample damping and Q_n^{o} is corrected for the free-to-contact frequency shift. This form of Q_n^{s} is striking because it is related to α and β , and not β alone, as illustrated in the Q_n^{s} vs α and β plots shown in Figure 3. From the plots, it is apparent that Q_n^{s} is not linearly proportional to β for any region of constant α . Furthermore, as is evident in Figure 3b, Q_n^{s} can decrease at constant β and increasing α . To validate the model, CRFM data were taken on PP and PS using the second and third eigenmodes n of the cantilever and loads ranging from 100 nN to 1 μ N. The results show that Q_n^{s} changes with the different applied loads (i.e., different α values) but that all data can be fit with a single β value, which is to be expected given the small changes in f_n^{c} at different α .

Loss Tangent. More recently, another CRFM method has been developed to measure the viscoelastic loss tangent $\tan \delta = E''/E'$.^{46,47} The main advantage to this method is that the expression for $\tan \delta$ is derived directly from Euler–Bernoulli beam mechanics and does not require an intermediate calculation of E' and E'' , thereby negating the need for calibration measurements on a material with known properties. It originates from the basic definition for $\tan \delta$ from instrumented indentation^{96,97}

$$\tan \delta = \frac{2\pi f_n^{\text{c}} c}{k} \quad (6)$$

Equation 6 can be combined with expressions for $x_n^{\text{o}}L$ and k_L to express $\tan \delta$ in terms of α and β

$$\tan \delta = \frac{(x_n^{\text{o}}L)^2 \gamma^2 \beta f_n^{\text{c}}}{\alpha f_n^{\text{o}}} \quad (7)$$

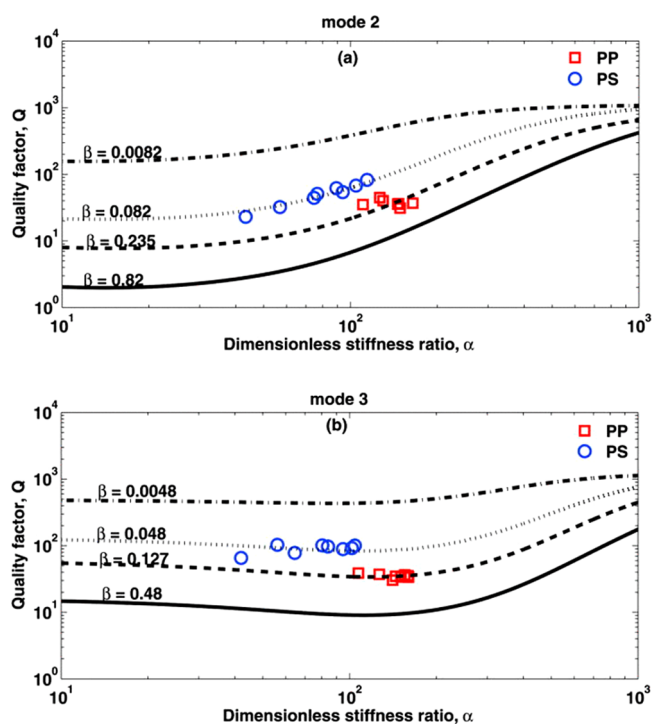


Figure 3. Experimental (symbols) and predicted (solid lines) quality factors Q_n^{s} for the (a) second and (b) third eigenmodes on PP and PS as a function of sample contact stiffness α for various values of sample damping β . It is important to note that Q_n^{s} changes with applied load, even along a constant β curve. Reproduced with permission from ref 45. Copyright 2011 American Institute of Physics.

As previously noted, eq 7 does not require calibration measurements on a material with known E' and E'' , only the measured values for f_n^{o} and f_n^{c} , $x_n^{\text{o}}L$ from the characteristic equation for free flexural resonance, α and β from eqs 1 and 2, and γ from the “mode-crossing” approach. Contour plots based on eq 7 yield another important conclusion: $\tan \delta$ is inversely related to Q_n^{c} but is also highly dependent on $f_n^{\text{c}}/f_n^{\text{o}}$.⁴⁷ As a result, the authors noted that it may be misleading to make predictions on $\tan \delta$ based solely on Q_n^{c} in multicomponent materials with a large range of f_n^{c} values. The method was tested on four polymer samples: PS, PE, and two commercial photostress polymers. In general, CRFM values for $\tan \delta$ were within a factor of 2 or 3 of literature values,^{98–100} with differences attributed to technique-to-technique variability in length scale, strain, and strain rate. Notably, PE showed the smallest frequency dependence from bulk mechanical testing and exhibited excellent agreement with CRFM as shown in Figure 4. It is important to note that such comparisons are only possible via time–temperature superposition (TTS), given the gaps in measurement frequencies. In this case, TTS¹⁰¹ was utilized to generate master curves with a reference temperature of 20 °C. The corresponding shift factors were then used to determine activation energies (assuming Arrhenius-type behavior), such that low-frequency dynamic mechanical analysis (DMA) data could be compared to higher frequency CRFM results. It is often more valuable to reverse the process (i.e., translate higher frequency CRFM results to lower frequency properties) because the time scales are more relevant to the polymer science community.

The Arnold group and collaborators pursued a similar analysis for evaluating internal friction, which is mathematically

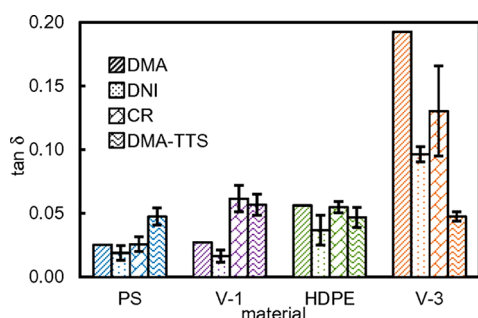


Figure 4. Loss tangent $\tan \delta$ results for four polymer samples: PS, PE, and two photostress polymers V-1 and V-3. DMA represents single dynamic mechanical analysis measurements at 10 Hz and 20 °C. DMA-TTS represents average values at 1 MHz through time-temperature superposition analysis of the DMA data. DNI represents dynamic nanoindentation measurements averaged from 10 to 300 Hz. CR represents CRFM data at 1.2 MHz. Reproduced with permission from ref 47.

identical to $\tan \delta$, in metallic glasses. Initially, Caron and Arnold¹⁰² treated the cantilever as a point-mass oscillator. The authors observed an increase in $1/Q_i^c$ with load, an effect that could be reversed on unloading suggesting heterogeneous dislocation nucleation. In subsequent work, the authors adopted the approach of Yuya et al.^{44,45} to improve the quantitative accuracy of their analysis. On amorphous PdCuSi metallic glass, Wagner et al.¹⁰³ showed good agreement between viscoelastic CRFM results and published data based on bulk measurements, corroborating the notion of decreased dissipation as PdCuSi goes from amorphous to crystalline.

■ VISCOELASTIC PROPERTY MAPPING

Mapping Techniques. These single point measurements can be repeated over an area on a sample to assess spatial variations in viscoelastic properties, but such an approach is often too time-consuming. As a result, recent work has focused on reducing the image acquisition time through the development of techniques such as phase-locked loop (PLL) detection,^{57,58} dual ac resonance tracking (DART),^{59–61} band excitation (BE),⁶² scanning probe resonance image tracking electronics (SPRITE),^{63,64} and FASTForce Volume CR.⁶⁵ Generally, the methods are placed into two categories: discrete or full-spectrum. In discrete methods, f_n^c and Q_i^c are determined using one or two points from the frequency response, while in full-spectrum methods, f_n^c and Q_i^c are taken from the entire response.

PLL and DART are examples of discrete methods for measuring f_n^c and Q_i^c . In PLL detection, the phase shift $\Delta\phi$ between the excitation and response signals is used to track f_n^c , and the amplitude A of the resonance peak is used to approximate Q_i^c . Yamanaka et al.⁵⁷ suggested that the A to Q_i^c estimation is straightforward, given that the two quantities exhibit a linear relationship over a large β range. As an application, the authors investigated a carbon-fiber-reinforced plastic composite as shown in Figure 5. The resonance frequency increased from f_n^0 at 38.5 kHz to f_n^c at 176 kHz for the carbon and 171 kHz for the epoxy, whereas Q_i^c were found to be 180–200 for the carbon and 100–110 for the epoxy. Thus, it was concluded that the epoxy was softer and more viscous than the carbon. More importantly, the f_n^c and Q_i^c maps revealed that both quantities were smaller in the core of the carbon than at the perimeter, which was attributed to radial

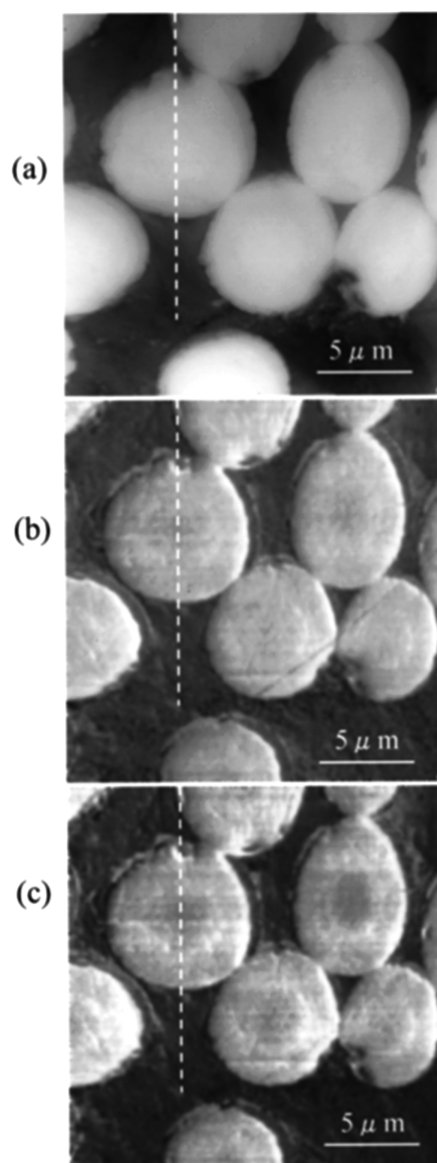


Figure 5. (a) Topography and first contact (b) resonance frequency f_n^c and (c) quality factor Q_i^c images of carbon-fiber-reinforced plastic composite. In (a), the maximum height difference is 500 nm, while in (b) and (c), the gray scales range from 170 to 180 kHz and 70 to 250, respectively. Reproduced with permission from ref 57. Copyright 2001 American Institute of Physics.

differences in the degree of stabilization during processing. Stan et al.⁵⁸ further developed the PLL detection method as it relates to CRFM to examine f_n^c and A in copper interconnects and low- k dielectric films at different applied loads. Using Cu as the calibration material, the f_n^c data indicated that the indentation modulus for the patterned low- k dielectric films (25 ± 3 GPa) was much larger than that for the blanket low- k dielectric films (10–12 GPa),¹⁰⁴ which was attributed to a structural densification during patterning. In contrast, the amplitude data were less quantitative (i.e., did not yield values for E' , E'' , or $\tan \delta$) but suggested a possible depth dependence in the contact damping. Notably, we now know that vibrational shape-related effects will also affect A with changing f_n^c and thus approximating Q_i^c by A must be treated carefully. This renders single-frequency PLL methods less useful for viscoelastic measurements versus elastic measurements.

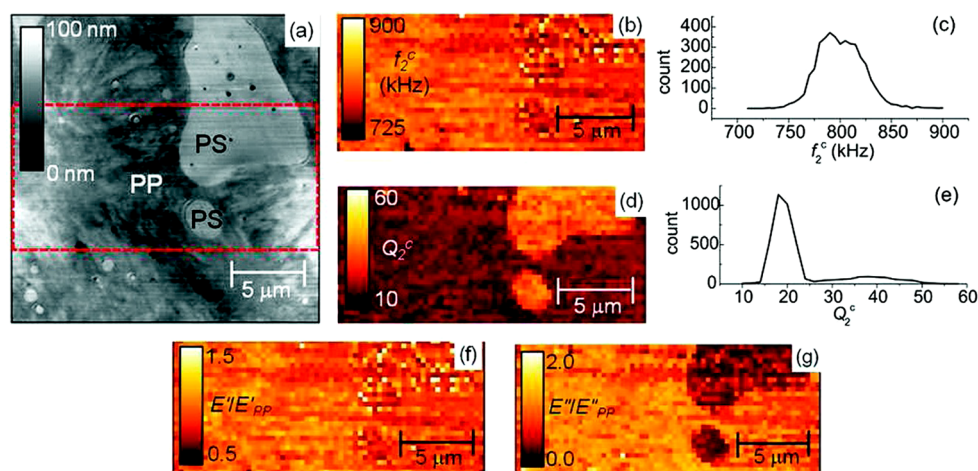


Figure 6. (a) Topography image of the PS–PP blend. Data flattened with a first-order line fit. The red box denotes the cropped region shown in (b), (d), (f), and (g). f_2^c (b) map and (c) histogram. Q_2^c (d) map and (e) histogram. (f) E'/E'_{pp} and (g) E''/E''_{pp} maps. E'_{PS}/E'_{PP} and E''_{PS}/E''_{PP} values from CRFM were in good agreement with DMTA data. Reproduced with permission from ref 106.

In DART, the tip–sample contact is modulated at two frequencies f_1 and f_2 , which are selected to surround f_n^c with some fixed $\Delta f = f_2 - f_1$ on the order of the full width at half-maximum of the resonance. At f_1 and f_2 , the amplitude (A_1 and A_2) and phase (ϕ_1 and ϕ_2) of the resonance peak are assessed. A feedback loop is used to set $A_2 - A_1 = 0$ by varying f_1 , ensuring that the resonance is between the two frequencies. After image acquisition, the precise f_n^c and Q_n^c are obtained by fitting results to a damped harmonic oscillator function. Rodriguez et al.^{59,60} developed the DART methodology to study local bias-induced phase transitions in ferroelectric materials via piezoresponse force microscopy (PFM). Gannepalli et al.⁶¹ later adopted the method to conduct nanoscale mapping of f_n^c and Q_n^c for DNA on mica and a binary PS/PP blend. For the DNA on mica, the results indicated smaller values for both f_n^c and Q_n^c for the DNA relative to the mica, which was attributed to a smaller contact stiffness and larger dissipation for DNA. For the PS/PP blend, the nanoscale maps revealed a large difference in Q_n^c , but only a small difference in f_n^c between the PS and PP regions, both of which are consistent with DMA data that point to large differences in E'' and small differences in E' for the two materials.

In contrast, BE, SPRITE, and FASTForce Volume CR are examples of full-spectrum methods for measuring f_n^c and Q_n^c . In BE, the excitation signal to the AFM cantilever is digitally synthesized with a predefined amplitude and phase within a given frequency window. The response of the cantilever is detected in contact with the sample and Fourier transformed to generate A and ϕ curves at each pixel in the image. The curves at each pixel are then fit to a simple harmonic oscillator model to create the f_n^c and Q_n^c maps. Jesse et al.⁶² validated the efficacy of the approach using simple theoretical and experimental examples. In one of the theoretical examples, the authors noted that for a resonance peak with $f_n^c = 150$ kHz and $Q_n^c = 200$ the width of the peak is ≈ 750 Hz, which would allow for sufficient sampling of the peak via the described methodology and hardware. This sampling efficiency increases as f_n^c increases and Q_n^c decreases. Experimentally, BE was coupled with magnetic force microscopy (MFM) to examine spatial variations in f_n^c and Q_n^c in yttrium–iron garnet. The f_n^c and Q_n^c maps exhibited flower-like and circular patterns,

respectively, in good agreement with results from standard MFM.¹⁰⁵

In SPRITE, a swept-frequency sine wave signal (i.e., a chirp) is applied to an actuator beneath the sample or another excitation source, and the root-mean-square amplitude response of the cantilever from the photodiode is converted to a direct-current voltage at each frequency and sampled with an analog-to-digital converter (ADC).^{63,64} The ADC output is then sent to a digital signal processor, which (1) stores the frequency response at each pixel, (2) fits the frequency response to a quadratic to determine f_n^c and Q_n^c , and (3) optionally uses the calculated value for f_n^c in a feedback-control loop to recenter the subsequent frequency sweep. Kos et al.⁶⁴ recently used SPRITE to create f_n^c and Q_n^c maps of an *Arabidopsis* plant. The maps demonstrated material property heterogeneities between the cell lumen and walls; in particular, the cell lumen exhibited smaller f_n^c and larger Q_n^c than the cell walls. Additional property heterogeneities were observed within the cell walls, likely from variations in the cellulose, lignin, and hemicellulose compositions. The more recent implementation allowed for the ability to chirp two frequency ranges to map two eigenmodes simultaneously. From these general descriptions, it is evident that there are several differences between SPRITE and BE in terms of their motivation and implementation. SPRITE was solely developed for CRFM and is therefore based on the application of a swept-frequency sine wave in the time domain. In contrast, BE was developed to enable a family of novel scanning probe techniques (e.g., PFM, MFM, and CRFM) and therefore is based on a generic predefined amplitude and phase signal processed in the time and frequency domains. SPRITE has recently demonstrated real-time polynomial curve fitting to calculate f_n^c and Q_n^c , thereby enabling *in situ* f_n^c and Q_n^c mapping and precluding the need to retain a complete set of frequency spectra for postprocessing.⁶⁴ Despite the differences, both SPRITE and BE enable f_n^c and Q_n^c mapping at multiple n at speeds much faster than a collection of point measurements.

In FASTForce Volume CR, the AFM cantilever is brought into contact with a sample surface at each point in an area, held at a constant applied force while the frequency is swept up to 5 MHz to collect the frequency response, and then retracted from the sample surface. Typically, this approach would not

enable any benefits over the point-by-point measurements described earlier. However, by leveraging fast-force spectroscopy and fast frequency sweeps, this methodology has been streamlined to generate 256×256 pixel property maps from a single eigenmode in under 30 min. The combined CRFM and force–volume tactic allows adhesion, elastic properties, and viscoelastic properties to be assessed in a single pass. Pittenger and Yablon validated the approach on both soft, viscoelastic (i.e., PP, PE, and PS) and stiff, elastic (i.e., Si, Al, and Cr) materials.⁶⁵

It is important to mention that several of the viscoelastic property mapping techniques outlined above have become commercially available. Oxford Instruments (Asylum Research) has added both the DART and BE implementations to the NanomechPro Toolkit on their MFP-3D and Cypher AFM platforms. Similarly, Bruker has added FASTForce Volume CR to the NanoMechanics Lab on their Dimension FastScan and Icon platforms. Moreover, Anasys Instruments has integrated CRFM into their Lorentz Contact Resonance and Resonance enhanced AFM-IR products, and NT-MDT has a CRFM toolbox that should allow for viscoelastic property measurements.

Property Maps. The previous studies were successful in providing the basis for viscoelastic property mapping but largely stopped short of affording guidance into the calculation of fundamental properties such as E' , E'' , and $\tan \delta$. Also, as discussed above, attempts to correlate Q_n^c with material damping can be problematic without consideration of the beam dynamics. Killgore et al.¹⁰⁶ developed the framework for this process, using pixel-by-pixel point maps and DART to assess f_n^c and Q_n^c and eqs 1–4 to determine E' and E'' for a PS/PP blend. The binary blend exhibited a continuous PP phase with PS domains ranging in size from 1 to 20 μm , as shown in Figure 6a. From the f_n^c and Q_n^c point maps and histograms in Figures 6b to 6e, there is a small f_n^c contrast but a large Q_n^c contrast, qualitatively implying similar elastic stiffnesses but different damping characteristics for the two phases (the interpretation of Q_n^c is valid here because of the similarity in f_n^c). Using PP as the calibration material (i.e., assuming bulk properties for PP), the relative storage $E'_{\text{PS}}/E'_{\text{PP}}$ and loss $E''_{\text{PS}}/E''_{\text{PP}}$ moduli for PS were assessed, yielding average values of $E'_{\text{PS}}/E'_{\text{PP}} = 0.95 \pm 0.20$ and $E''_{\text{PS}}/E''_{\text{PP}} = 0.34 \pm 0.16$ as shown in Figures 6f and 6g. For comparison, dynamic mechanical tensile analysis (DMTA) was performed on the PP and PS samples. After the TTS analysis, the DMTA measurements resulted in $E'_{\text{PS}}/E'_{\text{PP}} = 0.85$ and $E''_{\text{PS}}/E''_{\text{PP}} = 0.37$, in good agreement with CRFM results. Interestingly, the authors also assessed $E'_{\text{PS}}/E'_{\text{PP}}$ and $E''_{\text{PS}}/E''_{\text{PP}}$ as a function of scan velocity in DART and noted significant increases to both the absolute values and scatter in the data as velocity increased. These trends were qualitatively explained through material, contact mechanics, and instrumentation effects, but future work will focus on quantitatively accounting for these phenomena to improve the accuracy of CRFM for viscoelastic measurements while scanning.

In a follow-up study, Yablon et al.⁶⁶ sought to compare BE and DART to determine the effect of the measurement method on both the accuracy and timeliness of the viscoelastic property results. The initial comparison was conducted on a ternary blend of PP, PE, and PS. In both modes, f_n^c and Q_n^c were determined at each image pixel and then used to calculate α and β via eqs 1 and 2 and E' and E'' via eqs 3 and 4, using PP as the calibration. From the DART results, $E'_{\text{PS}}/E'_{\text{PP}}$ and $E''_{\text{PS}}/E''_{\text{PP}}$ were found to be 1.06 and 0.57, respectively, both of which

are in good agreement with the results from Killgore et al.¹⁰⁶ From the BE method images, $E'_{\text{PS}}/E'_{\text{PP}}$ and $E''_{\text{PS}}/E''_{\text{PP}}$ were shown to be ≈ 1 and 0.29, respectively. In both cases, the values for $E'_{\text{PS}}/E'_{\text{PP}}$ were in relatively good agreement with bulk DMA results, which yielded $E'_{\text{PS}}/E'_{\text{PP}}$ of 1.14. However, the $E''_{\text{PS}}/E''_{\text{PP}}$ values from the three methods were disparate, with the DMA data ($E''_{\text{PS}}/E''_{\text{PP}} = 0.24$) in much better agreement with the BE data than the DART data. Accordingly, BE provides more accurate data relative to the DART data, likely in large part because the extracted Q_n^c data are based on the entire frequency response and not just two points. However, this additional information comes at the expense of acquisition speed, which typically results in lower-resolution images in the BE mode. Yablon also studied a blend of PP and a rubbery elastomer. The storage modulus data were found to be unreliable on the elastomer because increased adhesion resulted in an exceptionally high contact area and thus CR frequency that could not be accommodated with a Hertzian contact model. The dissipative properties of the elastomer showed the expected trend in DART, but because of the low Q_n^c , the BE implementation failed.

Campbell et al.⁴⁶ used the point-by-point mapping routine from Killgore et al.¹⁰⁶ to assess the width and viscoelastic properties of the osteochondral interface between artificial calcified cartilage (ACC) and hyaline articular cartilage (HAC) in a white rabbit. Across the osteochondral interface, the average value for M' was found to decrease from 11.1 ± 2.4 GPa in the ACC to 6.1 ± 1.1 GPa in the HAC. The interface width w was determined from the very steep gradient in M' ; from multiple maps and line profiles, w was found to be 2.3 ± 1.2 μm , using the average M' in the ACC minus one standard deviation and the average M' in the HAC plus one standard deviation to define the boundary. In addition, the authors introduced the approach discussed above in eq 7 (albeit omitting a final tip-offset compensation) to generate $\tan \delta$ maps across the interface, as this method obviates the need for calibration measurements on a material with known properties. The value of $\tan \delta$ was shown to increase from 0.07 ± 0.04 in the ACC to 0.09 ± 0.03 in the HAC, with the gradient being much more gradual than that observed in the M' data. The $\tan \delta$ values from CRFM compared well with DMA,^{107,108} despite differences in sample preparation and measurement frequency. In contrast, the CRFM results for M' and w were about a factor of 2 less than those from instrumented indentation, both of which were explained in terms of the differences in probed volume of material between the two techniques.

Building off the approach of Campbell, Yablon et al.⁶⁷ utilized BE and DART to map $\tan \delta$ of a three-component blend of PP, PE, and PS. The focus of this study was twofold: (1) to study the viscoelastic properties of the polymer blend, but more notably, (2) to compare the aforementioned CRFM modes (i.e., DART and BE) to a recently developed amplitude modulation AFM (AM-AFM) mode¹⁰⁹ for $\tan \delta$ determination. In both CR modes, f_n^c and Q_n^c were determined at each image pixel and then used to calculate α and β via eqs 1 and 2 and $\tan \delta$ via eq 7. The average $\tan \delta$ values from DART for PP, PE, and PS were found to be 0.14 ± 0.01 , 0.11 ± 0.01 , and 0.06 ± 0.01 , respectively, indicating that the order of loss tangents is PP > PE > PS. BE-CRFM measurements on the same tertiary polymer blend and DMA data on bulk samples yielded a similar $\tan \delta$ trend, albeit with differences in the absolute values for each polymer. As before, the BE mode provided better agreement compared to bulk DMA data but

comes with the reduced scan speed and added complexity of fitting the entire frequency response as opposed to just two points in the DART mode. Arguably, the more interesting comparison is between $\tan \delta$ measured from the two CRFM methods and that calculated from the phase signal in AM-AFM.¹⁰⁹ In AM-AFM, the cantilever is in intermittent contact with the sample, with $\tan \delta$ measured in repulsive operation via knowledge of the free-oscillation amplitude, set point amplitude, and phase angle. The method is appealing because it mitigates the need to perform most of the experiments and calculations described above. However, the authors show that the $\tan \delta$ values from AM-AFM are in poor agreement with those from CRFM and DMA, both qualitatively in terms of the trends and quantitatively in terms of the absolute values. Potential reasons for the disagreements include method-to-method variability in the (1) linearity and frequency content of the tip-sample interactions and (2) source of the measured energy dissipation. In CRFM, the tip-sample interaction is linear, the drive is sinusoidal, and the energy is mainly dissipated in the sample, whereas in AM-AFM, the tip-sample interaction is nonlinear, the interaction forces have impulse-like loading, and energy is dissipated in both the sample and through longer range interactions.

■ ENVIRONMENTAL CONSIDERATIONS

With the basic viscoelastic CRFM technique reaching a certain level of maturity, considerable recent research in the field has looked toward extending the method to nonambient applications. These extensions can be broadly placed in two categories: (1) operating at elevated temperatures to perform thermomechanical analyses and (2) operating in environments where environmental damping of the cantilever dramatically affects CRFM damping (e.g., liquid operation).

Thermomechanical Analyses. Operation at elevated temperatures is a logical innovation for any polymer mechanical characterization method given the strong dependence of properties on temperature. Prior AFM methods have looked to assess thermomechanical properties with varying levels of quantification and accuracy. Many AFM methods such as force spectroscopy,¹¹⁰ phase imaging,¹¹¹ and FMM^{112,113} can identify the onset temperature of a thermomechanical transition (e.g., the melt temperature T_m or glass transition temperature T_g). The quantification of E' , E'' , or $\tan \delta$ over a temperature range is a more demanding pursuit that only recently has been addressed. With quantification also comes a more rigorous definition of transition temperatures; e.g., T_g is identified based on a nonmonotonic peak in the E'' versus T plot instead of a phenomenological increase in adhesion force or amplitude.¹¹⁴

Jesse et al.¹¹⁵ first demonstrated temperature-dependent viscoelastic CRFM using microresistively heated cantilevers, Joule expansion-based excitation, and the BE method of frequency and quality factor tracking. The authors immediately identified a critical challenge to thermomechanical property measurements—the rate at which the tip creeps into the sample increases significantly at elevated temperatures. Thus, a thermomechanical property measurement that involved engaging the surface at ambient temperature and then heating the tip through the material's transition temperature would result in a dramatically increasing contact area not described by elastic contact mechanics. The CR frequency could either decrease or increase depending on whether a reduction in storage modulus or increase in contact area dominated the

tip-sample interaction. To address this challenge, the authors performed a preindentation step where the tip was heated above the polymer's transition temperature, allowing a set amount of creep, and then cooled back to ambient temperature. Subsequent temperature changes below the initial indentation temperature did not lead to significant additional creep, allowing for unambiguous identification of material softening through the decrease in CR frequency and a nonmonotonic trend in the quality factor. For simplicity, the authors chose to model the cantilever as a point-mass simple harmonic oscillator, which may provide rank-order quantification of stiffness but does not generally provide adequate accuracy for quantitative property characterization. Nonetheless, the contact stiffness and damping coefficient were quantified, which can be used to calculate storage and loss modulus. Nikiforov et al.¹¹⁶ extended the approach to compare two excitation methods: periodic oscillations of the sample (as shown by Jesse et al.¹¹⁵) and periodic heating of the tip. The authors used both approaches to investigate the temperature-dependent properties of an amorphous and a semicrystalline polymer and compared the ensuing transition temperatures to those observed in differential scanning calorimetry (DSC) data. For the amorphous sample, both methods detected a glass-transition temperature of ≈ 85 °C, in good agreement with DSC results. For the semicrystalline sample, the glass-transition temperature was also detected along with an increase in the segment mobility just prior to the transition. In both samples, the transition region was better defined with periodic tip heating, leading to the conclusion that it was more effective method for detection.

More recently, multiple groups have combined sample-stage heating with a more rigorous beam model to perform loss tangent versus temperature measurements on polymer blends. As discussed above, the direct loss tangent calculation is independent of contact area and thus less sensitive to tip-sample creep artifacts. Chakraborty and Yablon¹¹⁷ used BE frequency and quality factor tracking in a pixel-by-pixel acquisition scheme to assess loss tangent on a PS/PP blend as shown in Figure 7. At room temperature, the authors reported $\tan \delta$ values in agreement with bulk DMA measurements adjusted with TTS to the CRFM frequency (≈ 300 kHz). As the blend was heated, $\tan \delta$ for both phases increased with temperature to a distinct maximum as shown in Figure 7c, beyond which the values decreased. In more detail, the PP exhibited a peak at 53 °C and the PS exhibited a peak at 75 °C. These transition temperatures were lower than those observed from DMA, prompting the authors to speculate about frequency-dependent effects on $\tan \delta$. The authors also reported significant thermal drift from heating of the sample, which will need to be addressed to observe temperature-dependent changes for a given region.

Natali et al.¹¹⁸ used a similar approach to characterize the temperature-dependent loss tangent of PS, PE, polycarbonate (PC), and a polymer-based nanocomposite from 25 to 70 °C. PS, PE, and PC were used as calibration samples to validate the approach over the temperature range; the resulting $\tan \delta$ values agreed with data from the literature both in terms of their absolute values and their trends with temperature. For the polymer-based nanocomposite (i.e., single-walled carbon nanotubes in an epoxy matrix), the authors studied the thermomechanical response with and without the nanotubes to determine their effect on the epoxy transition behavior. It was shown that the addition of the nanotubes reduced $\tan \delta$ by

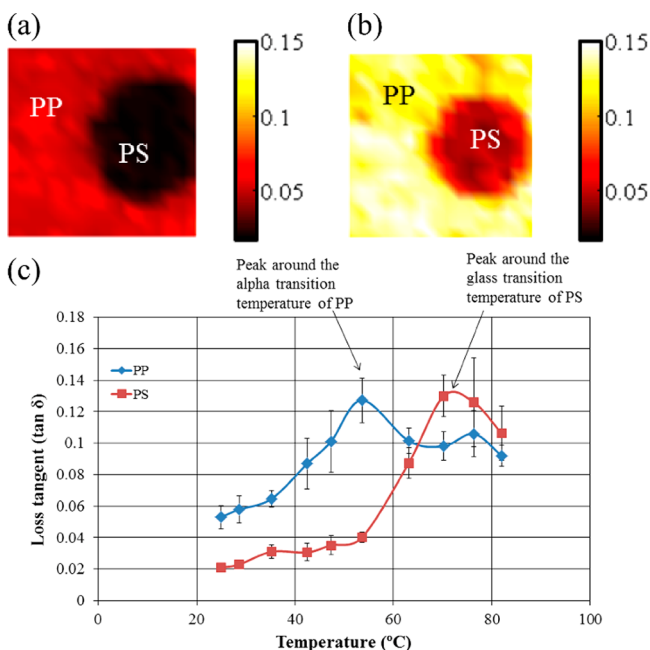


Figure 7. Loss tangent $\tan \delta$ maps for a PS–PP blend at (a) 25 °C and (b) 53 °C. (c) As the blend was heated, $\tan \delta$ for both phases increased with temperature to a distinct peak, beyond which the values decreased. In more detail, PP exhibited a peak at 53 °C and the PS exhibited a peak at 75 °C. Reproduced with permission from ref 117. Copyright 2014 Elsevier.

$\approx 60\%$ at room temperature; however, no differences in $\tan \delta$ were observed at 50 °C, suggesting that the viscoelastic response of the nanocomposite is dominated by the epoxy matrix at elevated temperatures. Overall, the determination of temperature-dependent loss tangent is proving to be a

promising application of viscoelastic CRFM technology that will likely see increased interest in the coming years.

Liquid Operation. The application of viscoelastic CRFM in liquid has also gained significant attention in recent years. Quantitative viscoelastic CRFM in liquids has demanded major innovations on cantilever excitation and modeling. Most viscoelastic and elastic contact resonance measurements to date have employed acoustic excitation at the sample or cantilever to excite the contact resonance. In liquids, this leads to substantial coupling of parasitic vibrations, which obscure the amplitude versus frequency data with a forest of peaks. This forest of peaks makes identification of the resonance frequency extremely difficult and accurate determination of the quality factor nearly impossible. So far, three methods have been used to circumvent the limitations of acoustic excitation for liquid viscoelastic CRFM: magnetic, Brownian motion, and photothermal excitation.

Parlak et al.¹¹⁹ compared acoustic excitation to magnetic excitation where a neodymium particle was adhered on backside of the cantilever and driven by a solenoid. The magnetically driven actuation resulted in a more Lorentzian peak shape, with a well-defined frequency and quality factor that shifted as predicted when the tip–sample contact stiffness was varied as shown in Figure 8a. The method proved suitable for liquid CRFM imaging of gold micropatterned with triethylene glycol mono-11-mercaptoundecyl ether (EG₃-thiol) regions as shown in Figure 9. The topography image was unable to clearly distinguish between the two regions, whereas the CRFM maps presented a decrease in f_3^c , an increase in Q_3^c , and a decrease in k for the EG₃-thiol relative to the gold substrate. Assuming a Hertzian contact and a reduced elastic modulus for the tip, the reduced elastic modulus for the gold and EG₃-thiol were found to be 59.8 ± 14.2 GPa and 51.3 ± 10 GPa, respectively. The former result was in good agreement with the bulk value for gold, while the EG₃-thiol

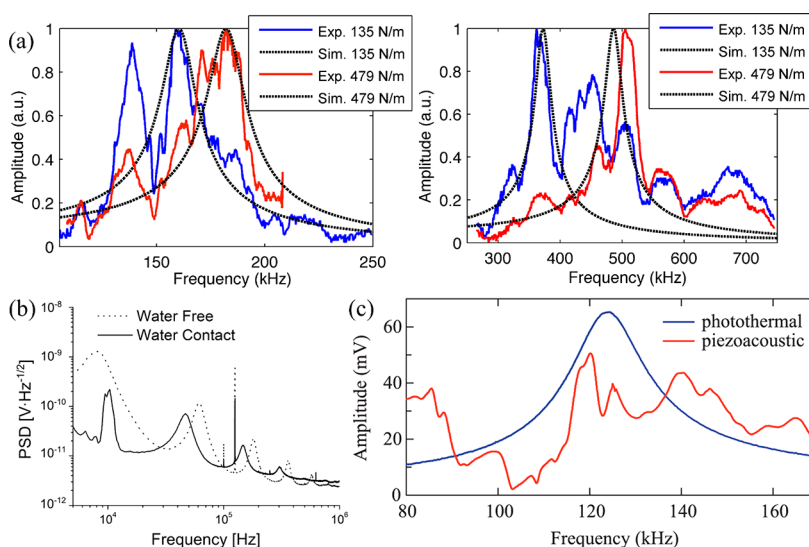


Figure 8. Cantilever excitation methods for viscoelastic CRFM in liquid environments. (a) Experimental and simulated contact resonance frequency spectra for the first (left) and second (right) eigenmodes at k of 135 and 479 N/m. The magnetically driven excitation was achieved via a neodymium particle adhered to the backside of the cantilever and driven by a solenoid. Reproduced with permission from ref 119. Copyright 2014 IOP Publishing. (b) Experimental free and contact frequency spectra for a cantilever actuated via the Brownian motion of the surrounding fluid. The peaks at 100 and 125 kHz are artifacts of the instrument controller, whereas the peaks at 10 kHz are noise. Reproduced with permission from ref 71. Copyright 2014 American Institute of Physics. (c) Experimental contact resonance frequency spectra for a cantilever actuated via piezoacoustic and photothermal excitation; the piezoacoustic signal exhibited multiple peaks, while the photothermal signal showed a clean peak at 124.1 kHz with a quality factor of 8.1. Reproduced with permission from ref 120. Copyright 2015 American Institute of Physics.

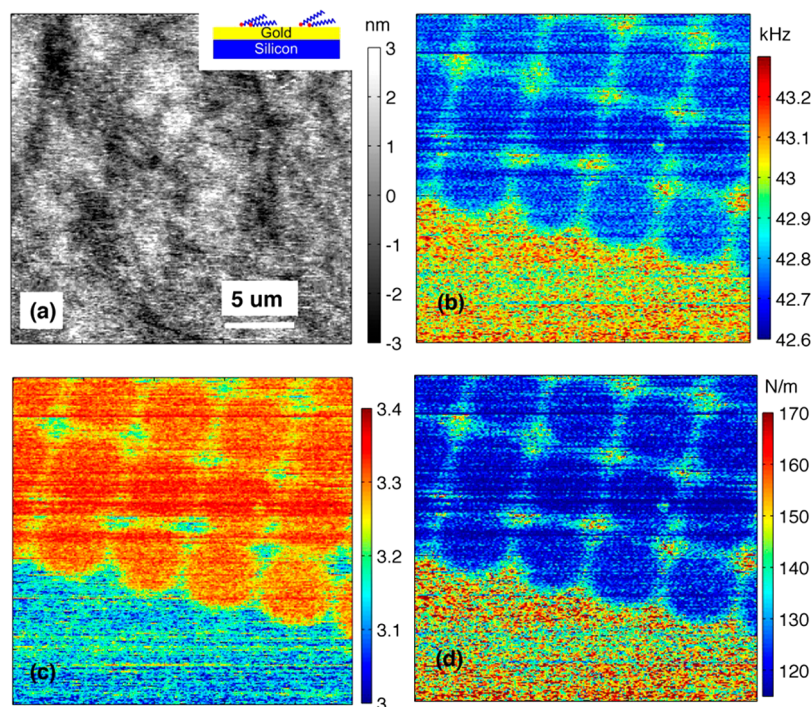


Figure 9. (a) Topography, (b) third contact resonance frequency f_3^c , (c) third contact quality factor Q_3^c , and (d) contact stiffness k for EG₃-thiol micropatterns on a gold surface in DI water. A sample schematic is shown as an inset in (a). The topography image was unable to clearly distinguish between the two regions, whereas the CRFM maps clearly presented a decrease in f_3^c , an increase in Q_3^c , and a decrease in k for the EG₃-thiol relative to the gold. Reproduced with permission from ref 119. Copyright 2014 IOP Publishing.

result indicates a compliant layer atop the stiffer gold. Quantitative measurement of the upper layer would require additional analyses to decouple the film–substrate properties.^{121–123} An even simpler excitation scheme was utilized by Tung et al.,⁷¹ wherein the cantilever was immersed in liquid and brought into contact with a glass slide. The Brownian motion of the surrounding fluid was sufficient to cleanly excite the first three contact resonance eigenmodes as shown in Figure 8b. Such an approach can be employed on nearly any AFM without modifications to the system or cantilever. The main limitations of the approach are (1) the signal-to-noise of the peaks drops off steeply with higher eigenmodes n due to increased dynamic stiffness and (2) the method requires several seconds to achieve a sufficient signal, limiting it to point spectra rather than imaging and complicating measurements subject to tip–sample creep. Kocun et al.¹²⁰ investigated the use of photothermal excitation for liquid viscoelastic CRFM. Photothermal excitation requires no modification to the cantilever and results in near-perfect Lorentzian peaks as shown in Figure 8c. The method was demonstrated in both air and water on two samples: a stiff Si wafer with Ti stripes and a softer PP/PE/PS blend. The authors observed good consistency between air and water measurements for both material sets, but their results tended to overpredict $\tan \delta$ in PS, a lower loss material.

Although it is tempting for simplicity to apply the same analysis used for CRFM in air to results obtained in water, neglecting the mass loading of the water and hydrodynamic function of the cantilever may lead to erroneous stiffness results and almost certainly will lead to erroneous damping results. Several groups^{119,124,125} have considered the hydrodynamics of the surface-coupled cantilever, but their analyses treated the fluid as unbounded, thus ignoring the important

fluid–structure interactions present in CRFM. A more complete model by Plosariu and Szoskiewicz¹²⁶ expands on the prior approaches by showing an experimental method for extracting the hydrodynamic function, but surface effects were still ignored. Recently, Tung et al.^{70,71} developed a relatively straightforward method of accounting for surface effects, cantilever shape effects, and the two-dimensional hydrodynamic function. The approach involves measuring the dry and liquid-immersed properties (i.e., f_n^0 and Q_n^0) of the freely vibrating cantilever near the sample surface and then using the theoretical form of the real and imaginary parts of the hydrodynamic function to determine the correction needed to account for the shape and frequency of the surface-coupled CRFM measurement. The real part of the hydrodynamic function Γ_r at a given frequency in liquid is given by

$$\Gamma_r(\text{Re}) = \frac{\left(\frac{f_n^0}{f_{n-\text{wet}}^0}\right)^2 - 1}{\tau} \quad (8)$$

where Re is the unsteady Reynolds number at a given frequency and f_n^0 and $f_{n-\text{wet}}^0$ are the dry and wet free resonance frequencies, respectively. The nondimensional parameter $\tau = \pi\rho_f b^2/4\rho A$, where ρ_f is the mass density of the surrounding fluid, ρ is the mass density of the beam, A is the cross-sectional area of the beam, and b is the width of the beam. The imaginary part of the hydrodynamic function Γ_i is then given by

$$\Gamma_i(\text{Re}) = \frac{\left(\frac{f_n^0}{f_{n-\text{wet}}^0}\right)^2}{\tau Q_{n-\text{wet}}^0} \quad (9)$$

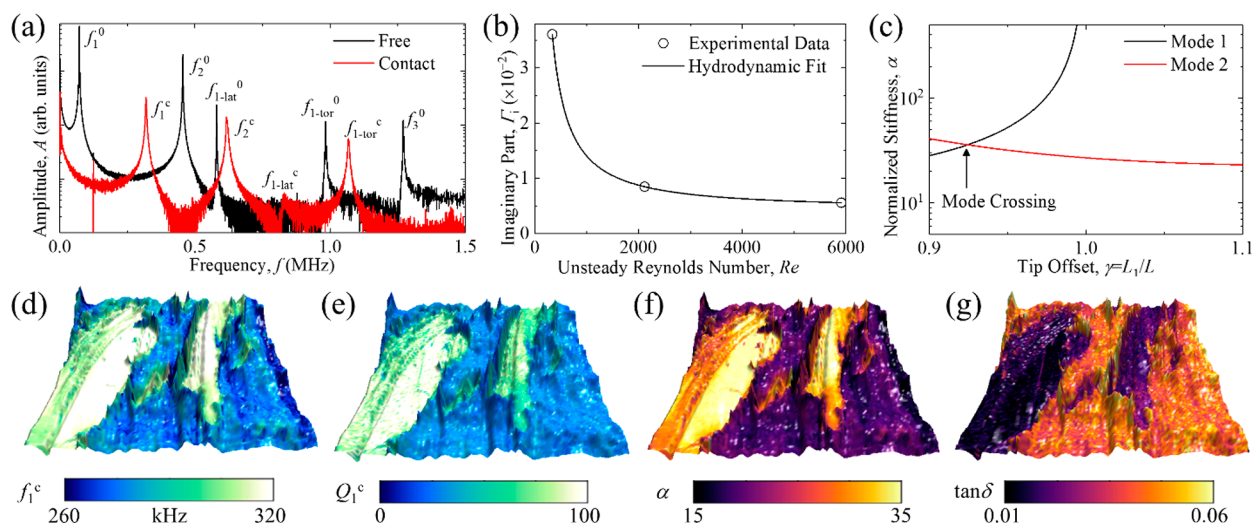


Figure 10. Complete viscoelastic CRFM data acquisition and analysis process using current best practices for a wood–polymer composite. (a) Free and contact resonance spectra for a cantilever driven via photothermal excitation. The peaks for the first four modes are Lorentzian in line shape, with little deviation from ideal behavior. (b) Experimental data and model fit to the imaginary part of the hydrodynamic function. The fit parameters inform the hydrodynamic correction to Q_i^c at a given f_n^c . (c) Tip-offset determination via the mode-crossing approach. In this example, the modes 1 and 2 α vs γ curves intersect at $\gamma = 0.924$, which is within the typically observed values of 0.90 and 1.05. Pixel-by-pixel point maps of (d) f_1^c , (e) Q_1^c , (f) α , and (g) $\tan \delta$ overlaid on a topography map of the wood–polymer composite. The lateral scan size is $10 \mu\text{m}$, and the full height range in the topography image is 840 nm. From the maps, it is clear that there are considerable differences in the properties of the wood fibers and the high-density polyethylene polymer.

where Q_{i-wet}^0 is the free quality factor of the immersed cantilever. The two parts of the hydrodynamic function allow the environmental damping to be interpolated and subtracted at the CR frequency. The approach was verified by Churnside et al.¹²⁷ on PS and PP, resulting in wet and dry $\tan \delta$ measurements that agreed within statistical error for specific eigenmodes. The utility of the approach was then demonstrated on a fixed sample of *Arabidopsis thaliana*; the resulting $\tan \delta$ image showed contrast between the primary cell walls, secondary cell walls, and middle lamella, in addition to $\tan \delta$ values in agreement with literature for cellulosic plant matter. Despite the initial application for liquid characterization, a simplified version only considering Γ_i also provides a robust and recommended method for separating sample and environmental damping in air.

■ STATE-OF-THE-ART AND BEST PRACTICES

The quality of elastic and viscoelastic CRFM measurements has improved dramatically in the 25 years since the inception of the technique. By combining the state-of-the-art technological and analytical methods, users can expect the highest accuracy in their measurements. Specifically, innovations in cantilever actuation, resonance acquisition, resonance tracking, and model design and range of applicability have resulted in measurement ease and accuracy that were not possible in the early days of the technique. In this section, we discuss what we feel are current best practices in terms of experiments and analysis for measurements of α and $\tan \delta$ performed in air environments.

Because of the strong dependence of the viscoelastic properties on Q_i^c , clean excitation of the cantilever is extremely important. Most early CRFM measurements employed acoustic excitation at either the cantilever holder or beneath the sample surface. Often, these actuation methods exhibit too many spurious vibrations for the lower Q_i , and amplitude of contact compared to free resonances. Heavily damped

actuators such as broadband fingertip ultrasound transducers can provide adequate signal, provided the sample is well affixed to the transducer and the sample itself does not exhibit resonances in the frequency range of interest. Not surprisingly, the actuation methods that have been successful in liquids (i.e., Brownian motion,⁷¹ magnetic,¹¹⁹ and photothermal¹²⁰) represent best practice for measurements in air because they retain a clean, artifact-free response. Other options that provide best-practice viscoelastic CRFM actuation include, but are not limited to, electrostatic⁵⁵ and Lorentz force excitation.³⁹ The benefits of direct excitation are especially evident for heavily damped materials (large $\tan \delta$) and when operating in heavily damped environments (e.g., in liquids). Also in regards to excitation, it is important to ensure that the tip–sample contact remains linear, as evidenced from the line shape of the resonance. A nonlinear resonance is evident from softening (skewing) of the resonance peak.¹²⁸ If nonlinearity is observed, the user must either reduce the drive amplitude or increase the set point force to ensure the tip–sample contact remains linear.

Mapping will generally require a trade-off between speed and absolute accuracy in f_n^c and Q_i^c . The fastest mapping techniques employ multifrequency feedback loops (e.g., DART) or phase-locked loops (e.g., PLL). However, these techniques must infer a resonance line shape from a limited number of observables. Full-spectrum methods (e.g., BE and SPRITE) provide a more accurate description of the cantilever dynamics, while making discrepancies between model to experiment more readily identifiable. A second decision is whether to continuously scan the surface in contact mode or perform a point-map where the probe is stationary during acquisition. We have repeatedly observed scan-related phenomena in CRFM (e.g., reduced f_n^c and Q_i^c) while scanning compared to stationary.^{106,129} Possible explanations include hydrodynamic and viscoelastic effects. Therefore, we recommend scanning when the highest spatial resolution for

viscoelastic mapping is required; however, we suggest point maps when striving for the most accurate viscoelastic property characterization.

Figure 10 shows an example of a complete data acquisition and analysis experiment for viscoelastic CRFM using our best practices. The chosen cantilever is an ≈ 3 N/m rectangular cantilever with a slight picket shape, and the sample is a wood–polymer composite which exhibits significant mechanical heterogeneity. The CR was driven photothermally with the excitation laser located near the base of the cantilever. Figure 10a shows representative free and CR spectra obtained on the sample. The resonances are Lorentzian in line shape, with little deviation from ideal behavior. By comparing the observed frequency ratios between free eigenmodes to those predicted theoretically $\{f_2^0/f_1^0, f_3^0/f_1^0, f_4^0/f_1^0, f_5^0/f_1^0\} = \{6.27, 17.55, 34.39, 56.84\}$, nonflexural resonances such as those at 580 and 983 kHz can be identified. The frequency range around the nonflexural free resonance should be treated cautiously when moving to contact because of concerns over energy transfer between modes. If adequate CR signal is not observed for some region of the sample, two approaches can be taken. First, as suggested by Figure 3, for a given damping, Q_c^i and thus the signal strength can be increased by operating at a higher value of α . This could be achieved by increasing the set point force or intentionally wearing the probe to increase its radius. Second, as shown experimentally in Figure 11, the amplitude of

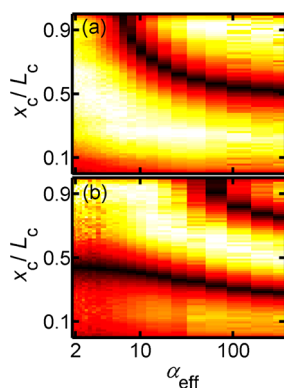


Figure 11. Cantilever slope amplitude as a function of normalized effective contact stiffness α_{eff} and relative position of laser spot x_c/L_c for $k_t \approx 2.7$ N/m and modes 1 to 2. The column has been normalized to vary between zero (black) and one (white) and represents the absolute value of the derivative of the vibrational shape at a given contact stiffness. The dark curves show the motion of the antinode positions. Reproduced with permission from ref 130. Copyright 2015 IOP Publishing.

the CR is dependent on the vibrational shape, which is dependent on α .¹³⁰ This indicates that for every value of α there is an optimal position for the detection laser as well as n laser positions that result in antinodes with no signal. By optimizing the laser position and α for the higher-loss-tangent region of the sample, it is possible to improve the overall odds of detection.

Figures 10d and 10e show 128×128 maps of f_1^i and Q_c^i overlaid on topography images acquired on a $10 \mu\text{m} \times 10 \mu\text{m}$ region of the sample. On this sample, DART imaging in contact mode tended to damage the softer high-density polyethylene (HDPE) domains, leading to erroneous Q_c^i results. Thus, data were acquired via point-by-point mapping with the tip fully withdrawn between pixels. Complete CR

spectra for the first eigenmode were acquired at every pixel. The amplitude A versus frequency f of the obtained free and contact resonance peaks were fit to a damped simple harmonic oscillator function

$$A(f) = \frac{f_n^2 A_{\text{drive}}}{\sqrt{(f_n^2 - f^2)^2 + (f_n f / Q_n)^2}} + C_1 f + C_2 \quad (10)$$

where A_{drive} is the drive amplitude. C_1 and C_2 are optional constants to account for baseline tilt and offset in the spectra. From the f_1^i map, considerable variation in the elastic properties can be inferred such as stiffness variation within the different cell wall types of the wood and the dramatic contrast compared with HDPE. The map of Q_c^i generally mimics the contrast observed in f_1^i , but care must be exercised to not overinterpret Q_c^i contrast as damping contrast because of the substantial variation in f_1^i . Thus, even qualitative assessment of viscoelastic properties requires further analysis.

First, the properties of the cantilever itself are characterized from the free and contact A versus f spectra. This includes the imaginary hydrodynamic function Γ_i and the tip offset position γ . Free and contact resonance spectra were acquired with sufficient bandwidth to encompass at least three free eigenmodes and two CR eigenmodes as shown in Figure 10a. The spectrum acquisition time was made sufficiently long that the sweeping rate did not exceed the response time of the cantilever. Typically, 60 s is adequate for characterizing a 2 MHz bandwidth. If the spectrum is swept too quickly, asymmetric distortion of the resonance peaks is observed, and the sweep width should be decreased. The free resonances are captured with the cantilever located as close as possible to the sample surface to approximate fluid–structure interactions that occur in the bounded fluid when the cantilever is in contact. Here, a F – d curve with a controlled pull-off distance of 300 nm was used to leave the probe tip close to the sample. Because the cantilever-to-sample distance is offset by the tip height (typically 5–15 μm), a 300 nm gap is negligible. For reasons discussed in the tip-offset calibration below, the CR spectrum is taken on a stiff region of the sample or with a higher force where an upper bound α and thus f_n^i is expected.

To account for the environmental damping acting on the cantilever, the imaginary part of the hydrodynamic function Γ_i is calculated from eq 9. The real part of the hydrodynamic correction is not needed for measurements in air. Figure 10b shows a fit to the imaginary hydrodynamic function for the first three free resonances of the cantilever. The fit function is

$$\Gamma_i(\text{Re}) = B_1 + B_2 \text{Re}^{-1/2} + B_3 \text{Re}^{-1} \quad (11)$$

where B_n are adjustable parameters in the fit. Remembering that Re is linearly proportional to f_1^i , eq 11 allows environmental damping effects to be subtracted from Q_c^i for every pixel of the image. Of note, the hydrodynamic correction is less dramatic at higher eigenmodes for a particular cantilever, but $n = 1$ was chosen here because it avoids any interaction with nonflexural resonances.

After fitting the hydrodynamic function of the cantilever, γ was calculated, given its impacts on the mass distribution and effective length of the cantilever. Tip offset was assessed by identifying the value of γ where α is identical for two eigenmodes measured and calculated under the same contact conditions. Figure 10c shows plots of α versus γ for $n = 1$ and 2 with the tip in contact with a wood portion of the sample. The

value of $\gamma = 0.924$ was determined graphically from the crossing shown in Figure 10c and mathematically by solving the minimum between the two curves. In general, the sensitivity of α to changes in γ is largest when α is large and n is small. Determining γ from a stiff portion of the sample ensures that nonphysical values for α are not encountered later in the analysis. The values of γ and α can also inform the user whether the beam model in eq 1 is suitable for their experimental conditions. Generally, values of γ between 0.9 and 1.05 are observed. If γ falls outside these boundaries or α is negative or unphysically high or low, it is likely that the contact is too stiff to model the chosen eigenmodes without consideration of lateral stiffness (i.e., the model in Figure 2e should be used). Likewise, if an eigenmode shows a large change in α for a small change in γ , that is an indication that the upper limit of applicability for eq 1 is being approached.

With knowledge of γ and Γ_{β} , f_1^i and Q_1^c maps can be processed into material property maps. First, $\Gamma_i(\text{Re})$ is evaluated at each pixel in the f_1^i map to determine the damping associated with the environment Q_{hydro} . Subsequently, the damping associated with the contact Q_1^c for each pixel can be calculated from

$$(Q_n^c)^{-1} = (Q_{\text{hydro}})^{-1} + (Q_n^s)^{-1} \quad (12)$$

By examination of eq 12, it is apparent that consideration of the hydrodynamic function is most important when Q_n^s is large. For lower Q_n^s , the influence of Q_{hydro} is often negligible. For the sample under investigation, the hydrodynamic correction accounts for an $\approx 8\%$ increase in Q on HDPE and an $\approx 30\%$ increase in Q on the wood.

With the corrected Q values, eq 1 can be used to calculate the normalized contact stiffness α and normalized contact damping β by taking the real and imaginary parts of the solution. Then, the maps of f_1^i , α , and β are evaluated on a pixel-by-pixel basis with eq 7 to determine $\tan \delta$. We calculated $\alpha = 33.3 \pm 2.8$ and $\alpha = 18.6 \pm 1.0$ on representative regions of the wood and HDPE, respectively. The contact stiffness values indicate a reduced modulus $\approx 2.4\times$ larger for the wood than the HDPE if assuming sphere-on-plane Hertzian contact. The elastic stiffness sensitivity of CRFM is highlighted by the contrast in α exhibited between the lower- α middle lamella and the higher- α secondary cell walls. In terms of viscoelastic properties, we calculated $\tan \delta = 0.018 \pm 0.004$ and $\tan \delta = 0.048 \pm 0.006$ on representative regions of the wood and HDPE, respectively. The value on wood is characteristic of glassy polymeric materials (e.g., PS) in the literature. The value on HDPE is in excellent agreement with our prior bulk measurements on homogeneous HDPE,⁴⁷ where $\tan \delta = 0.044$ was determined by TTS of DMA results to a frequency of 270 kHz. Table 1 includes a summary of measured and calculated values used to prepare Figure 10 that researchers can use to verify the accuracy of their viscoelastic CRFM analysis before applying it to unknown samples.

FUTURE DIRECTIONS

Despite the extensive progress made in viscoelastic CRFM thus far and outlined above, we still see potential for measurement advancement. In particular, the ability of viscoelastic CRFM to bring AFM spatial resolution to more of the characterization capabilities of bulk viscoelastic techniques is of interest. Already, we have seen examples of this with temperature-dependent material properties, but the viscoelastic CRFM

Table 1. Measured and Calculated Values To Verify Best Practice Viscoelastic CRFM Analysis

parameter	value
$\{f_1^0, f_2^0, f_3^0\}$	{72.68, 455.3, 1271} kHz
$\{Q_1^0, Q_2^0, Q_3^0\}$	{127, 542, 823}
$\{f_1^c, f_2^c\}$ for tip offset	{319.5, 618.5} kHz
tip offset γ	0.924
mean f_1^i in HDPE	274.1 kHz
mean Q_1^c in HDPE	29.3
mean Q_1^s in HDPE	31.6
mean α in HDPE	18.6
mean $\tan \delta$ in HDPE	0.048

method should be equally capable of characterizing photo-mechanical and other stimuli-sensitive responses. So far, thermomechanical measurements have exploited the spatial resolution of viscoelastic CRFM but have not yet considered the fast-temporal resolution that arises due to the kilohertz to megahertz resonance frequencies and comparatively small quality factors. Furthermore, we expect to see frequency-dependent properties explored more explicitly, either by exploiting the infinite number of vibrational eigenmodes in viscoelastic CRFM or by tailoring the properties of the cantilever, sample, or experiment to achieve a range of frequencies within a given eigenmode. These frequency-dependent measurements could improve on the accuracy and sensitivity of subresonance methods^{15,131–133} and inform more complex viscoelastic models than the Kelvin–Voigt element.¹³⁴

Additionally, we see potential for continued improvements in viscoelastic CRFM mapping capabilities. This direction should focus on removing the limitations imposed by continuous contact mode scanning as well as improving the accuracy of Q_n^c determination. Thus far, we have seen efforts to incorporate CRFM into subresonance intermittent-contact AFM modes such as pulsed force, time-resolved interaction force, or peak force tapping.^{33,135,136} These modes perform a sinusoidal $F-d$ curve at each pixel of the image at rates of hundreds of hertz to a few kilohertz. Typically, these modes are analyzed with just a quasistatic deflection signal, akin to low-frequency $F-d$ measurements; however, there is ample time during the contact portion of each $F-d$ curve to obtain complementary CRFM information. Parlak et al.¹³⁷ used a single-frequency drive close to f_n^c with an experimental calibration between amplitude and k to map elastic stiffness. Killgore and Hurley¹³⁵ later showed how a dual-frequency excitation in the vicinity of f_1^i , at fixed frequencies during a 200 Hz pulsed-force excitation, could allow extraction of f_n^c , Q_n^c , A_{drive} , and θ_{drive} versus F_{app} . This lays the foundation for viscoelastic mapping, although property extraction has not yet been realized. Also, a lack of a reliable pulsed-force feedback loop prevented broader expansion of this approach at the time. Finally, Stan and Gates¹³⁶ have recently shown incorporation of a PLL at f_1^i with peak force tapping. Their approach allowed for complete image acquisition, but the single-frequency PLL complicates Q_n^c determination. It remains to be seen whether integration with subresonance intermittent contact is beneficial to viscoelastic CRFM or whether it also introduces new complications that must be considered.

In terms of accurate Q_n^c determination, expanded use of multifrequency AFM methods could provide improved data reliability. This could come from wider access to full-spectrum

methods such as BE⁶² or from extensions of DART that utilize a greater number of observation frequencies to better quantify Q_i^c and its related uncertainties. Quantification of very low Q_i^c (e.g., $Q_i^c \leq 1$) is also of interest for the characterization of high $\tan \delta$ materials, but may require time-domain ring down analysis, rather than observation in the frequency domain.

Overall, between the extensive developments that have already taken place in viscoelastic CRFM and the potential for further measurement development and application dissemination, the method looks to be entering a productive time period for adoption and impact. With improved ease of use and more confidence in accuracy of property measurements, viscoelastic CRFM is well-poised to make the transition from characterization of calibration materials (e.g., PS, PP, and PE) to advanced materials, where it can inform materials discovery. As a means of investigating material properties in ambient conditions, we see significant potential in characterizing phenomena such as interfaces and interphases in composites^{138,139} and additively manufactured parts;^{140,141} domain properties in phase-separated blends and copolymers;^{142,143} viscoelastic properties of thin films and nanostructures;^{144,145} and high-frequency viscoelastic properties for crashworthiness and ballistics. In liquid environments, a host of additional applications arise including the characterization of engineered nanoscale materials for biondiagnostics and targeted drug delivery;^{146–148} extracellular matrix model materials for stem-cell-based therapeutics;^{149,150} and biological materials for tissue regeneration and repair.¹⁵¹ The continued advances in CRFM capabilities will only further enhance these advanced-materials applications.

AUTHOR INFORMATION

Corresponding Authors

*E-mail: jason.killgore@nist.gov.

*E-mail: frank.delrio@nist.gov.

ORCID

Frank W. DelRio: 0000-0003-1727-8220

Notes

The authors declare no competing financial interest.

Biographies



Jason P. Killgore earned a B.S. (2002) in Plastic Engineering Technology from Western Washington University before pursuing his M.S. (2005) and Ph.D. (2009) degrees in Chemical Engineering from the University of Washington. During his Ph.D. research, Jason used scanning probe microscopy (SPM) to characterize the properties and performance of polymeric gas separation membranes. Upon completion of his Ph.D., he received a National Research Council

fellowship award to develop nanomechanical SPM methods at the National Institute of Standards and Technology in Boulder, CO. Jason presently leads the Scanning Probe Microscopy for Advanced Materials and Properties project in the Applied Chemicals and Materials Division at NIST. His interests include the development of novel SPM instrumentation and methods to address characterization needs in manufacturing, energy, electronics, and advanced materials. Jason has authored more than 30 peer reviewed journal articles and 2 book chapters and serves as the associate editor for SPM submissions to *Ultramicroscopy*.



Frank W. DelRio received a B.S. in Mechanical Engineering from Carnegie Mellon University in 1998, after which he worked as a Product Support Engineer at C&D Aerospace (now C&D Zodiac). In 2001, he returned to academia, ultimately receiving an M.S. in Mechanical Engineering from Boise State University in 2002 and a Ph.D. in Mechanical Engineering from the University of Colorado at Boulder in 2006. After working as a postdoctoral researcher at the University of California, Berkeley, he joined the Materials Science and Engineering Laboratory (now Material Measurement Laboratory, MML) at the National Institute of Standards and Technology (NIST). At NIST, Frank has served as the Leader of the Nanoscale Strength Measurements and Standards Project from 2007 to 2014, as the Leader of the Small-Scale Mechanics for Advanced Materials Project from 2014 to 2016, and as a Science Advisor in the MML Lab Office from 2016 to 2017. Currently, he is the Leader of the Fatigue and Fracture Group, which conducts research on the fatigue and fracture of advanced structural materials for pipeline safety, hydrogen storage, additive manufacturing, and cardiac device reliability. His research focuses on the development of materials and assemblies for small-scale applications via advancements in stand-alone and integrative mechanical measurement and microscopy methods, with an emphasis on advanced materials in electronics, biomedical and health, infrastructure, energy, and forensics applications. Frank is the recipient of several awards and honors, including the ASME Orr Early Career Award, Department of Commerce Bronze Medal Award, SEM A.J. Durelli Award, and Presidential Early Career Award for Scientists and Engineers.

ACKNOWLEDGMENTS

Specific commercial equipment, instruments, and materials that are identified in this report are listed in order to adequately describe the experimental procedure and are not intended to imply endorsement or recommendation by the National Institute of Standards and Technology (NIST).

REFERENCES

- (1) Lakes, R. *Viscoelastic Materials*; Cambridge University Press: 2009.

- (2) Oyen, M. L. *Handbook of Nanoindentation: With Biological Applications*; Pan Stanford Publishing: Singapore, 2011.
- (3) Oliver, W. C.; Pharr, G. M. An improved technique for determining hardness and elastic modulus using load and displacement sensing indentation experiments. *J. Mater. Res.* **1992**, *7* (6), 1564–1583.
- (4) Oliver, W. C.; Pharr, G. M. Measurement of hardness and elastic modulus by instrumented indentation: Advances in understanding and refinements to methodology. *J. Mater. Res.* **2004**, *19* (1), 3–20.
- (5) Tsukruk, V. V.; Singamaneni, S. *Scanning Probe Microscopy of Soft Matter: Fundamentals and Practices*; Wiley-VCH Verlag GmbH & Co. KGaA: Weinheim, Germany, 2012.
- (6) Dufrene, Y. F.; Ando, T.; Garcia, R.; Alsteens, D.; Martinez-Martin, D.; Engel, A.; Gerber, C.; Müller, D. J. Imaging modes of atomic force microscopy for application in molecular and cell biology. *Nat. Nanotechnol.* **2017**, *12*, 295.
- (7) Wang, D.; Russell, T. P. Advances in Atomic Force Microscopy for Probing Polymer Structure and Properties. *Macromolecules* **2018**, *51* (1), 3–24.
- (8) Burnham, N. A.; Colton, R. J. Measuring the nanomechanical properties and surface forces of materials using an atomic force microscope. *J. Vac. Sci. Technol., A* **1989**, *7* (4), 2906–2913.
- (9) Chizhik, S. A.; Huang, Z.; Gorbunov, V. V.; Myshkin, N. K.; Tsukruk, V. V. Micromechanical Properties of Elastic Polymeric Materials As Probed by Scanning Force Microscopy. *Langmuir* **1998**, *14* (10), 2606–2609.
- (10) Butt, H.-J.; Cappella, B.; Kappl, M. Force measurements with the atomic force microscope: Technique, interpretation and applications. *Surf. Sci. Rep.* **2005**, *59* (1–6), 1–152.
- (11) Rosa-Zeiser, A.; Weilandt, E.; Hild, S.; Marti, O. The simultaneous measurement of elastic, electrostatic and adhesive properties by scanning force microscopy: pulsed-force mode operation. *Meas. Sci. Technol.* **1997**, *8* (11), 1333.
- (12) Young, T. J.; Monclus, M. A.; Burnett, T. L.; Broughton, W. R.; Ogin, S. L.; Smith, P. A. The use of the PeakForce TM quantitative nanomechanical mapping AFM-based method for high-resolution Young's modulus measurement of polymers. *Meas. Sci. Technol.* **2011**, *22* (12), 125703.
- (13) Dokukin, M. E.; Sokolov, I. Quantitative mapping of the elastic modulus of soft materials with HarmoniX and PeakForce QNM AFM modes. *Langmuir* **2012**, *28* (46), 16060–16071.
- (14) He, C.; Shi, S.; Wu, X.; Russell, T. P.; Wang, D. Atomic Force Microscopy Nanomechanical Mapping Visualizes Interfacial Broadening between Networks Due to Chemical Exchange Reactions. *J. Am. Chem. Soc.* **2018**, *140* (22), 6793–6796.
- (15) Maivald, P.; Butt, H. J.; Gould, S. A. C.; Prater, C. B.; Drake, B.; Gurley, J. A.; Elings, V. B.; Hansma, P. K. Using force modulation to image surface elasticities with the atomic force microscope. *Nanotechnology* **1991**, *2* (2), 103.
- (16) Lozano, J. R.; Garcia, R. Theory of multifrequency atomic force microscopy. *Phys. Rev. Lett.* **2008**, *100* (7), 076102.
- (17) Raman, A.; Melcher, J.; Tung, R. Cantilever dynamics in atomic force microscopy. *Nano Today* **2008**, *3* (1), 20–27.
- (18) Garcia, R.; Herruzo, E. T. The emergence of multifrequency force microscopy. *Nat. Nanotechnol.* **2012**, *7*, 217.
- (19) Rabe, U.; Arnold, W. Acoustic microscopy by atomic force microscopy. *Appl. Phys. Lett.* **1994**, *64* (12), 1493–1495.
- (20) Yamanaka, K.; Nakano, S. Ultrasonic Atomic Force Microscope with Overtone Excitation of Cantilever. *Jpn. J. Appl. Phys.* **1996**, *35* (6S), 3787.
- (21) Rabe, U.; Amelio, S.; Kester, E.; Scherer, V.; Hirsekorn, S.; Arnold, W. Quantitative determination of contact stiffness using atomic force acoustic microscopy. *Ultrasonics* **2000**, *38* (1), 430–437.
- (22) Hurley, D. C.; Turner, J. A. Measurement of Poisson's ratio with contact-resonance atomic force microscopy. *J. Appl. Phys.* **2007**, *102* (3), 033509.
- (23) Rabe, U.; Kopycinska, M.; Hirsekorn, S.; Saldaña, J. M.; Schneider, G. A.; Arnold, W. High-resolution characterization of piezoelectric ceramics by ultrasonic scanning force microscopy techniques. *J. Phys. D: Appl. Phys.* **2002**, *35* (20), 2621.
- (24) Passeri, D.; Bettucci, A.; Germano, M.; Rossi, M.; Alippi, A.; Orlanducci, S.; Terranova, M. L.; Ciavarella, M. Effect of tip geometry on local indentation modulus measurement via atomic force acoustic microscopy technique. *Rev. Sci. Instrum.* **2005**, *76* (9), 093904.
- (25) Stan, G.; Price, W. Quantitative measurements of indentation moduli by atomic force acoustic microscopy using a dual reference method. *Rev. Sci. Instrum.* **2006**, *77* (10), 103707.
- (26) Kester, E.; Rabe, U.; Presmanes, L.; Tailhades, P.; Arnold, W. Measurement of Young's modulus of nanocrystalline ferrites with spinel structures by atomic force acoustic microscopy. *J. Phys. Chem. Solids* **2000**, *61* (8), 1275–1284.
- (27) Geer, R. E.; Kolosov, O. V.; Briggs, G. A. D.; Shekhawat, G. S. Nanometer-scale mechanical imaging of aluminum damascene interconnect structures in a low-dielectric-constant polymer. *J. Appl. Phys.* **2002**, *91* (7), 4549–4555.
- (28) Kopycinska-Müller, M.; Geiss, R. H.; Müller, J.; Hurley, D. C. Elastic-property measurements of ultrathin films using atomic force acoustic microscopy. *Nanotechnology* **2005**, *16* (6), 703.
- (29) Zheng, Y.; Geer, R. E.; Dovidenko, K.; Kopycinska-Müller, M.; Hurley, D. C. Quantitative nanoscale modulus measurements and elastic imaging of SnO₂ nanobelts. *J. Appl. Phys.* **2006**, *100* (12), 124308.
- (30) Stan, G.; Krylyuk, S.; Davydov, A. V.; Cook, R. F. Compressive Stress Effect on the Radial Elastic Modulus of Oxidized Si Nanowires. *Nano Lett.* **2010**, *10* (6), 2031–2037.
- (31) Tsuji, T.; Yamanaka, K. Observation by ultrasonic atomic force microscopy of reversible displacement of subsurface dislocations in highly oriented pyrolytic graphite. *Nanotechnology* **2001**, *12* (3), 301.
- (32) Sarioglu, A. F.; Atalar, A.; Degertekin, F. L. Modeling the effect of subsurface interface defects on contact stiffness for ultrasonic atomic force microscopy. *Appl. Phys. Lett.* **2004**, *84* (26), 5368–5370.
- (33) Parlak, Z.; Degertekin, F. L. Contact stiffness of finite size subsurface defects for atomic force microscopy: Three-dimensional finite element modeling and experimental verification. *J. Appl. Phys.* **2008**, *103* (11), 114910.
- (34) Hurley, D. C.; Kopycinska-Müller, M.; Langlois, E. D.; Kos, A. B.; Barbosa, N., III Mapping substrate/film adhesion with contact-resonance-frequency atomic force microscopy. *Appl. Phys. Lett.* **2006**, *89* (2), 021911.
- (35) Killgore, J. P.; Kelly, J. Y.; Stafford, C. M.; Fasolka, M. J.; Hurley, D. C. Quantitative subsurface contact resonance force microscopy of model polymer nanocomposites. *Nanotechnology* **2011**, *22* (17), 175706.
- (36) Kimura, K.; Kobayashi, K.; Yao, A.; Yamada, H. Visualization of subsurface nanoparticles in a polymer matrix using resonance tracking atomic force acoustic microscopy and contact resonance spectroscopy. *Nanotechnology* **2016**, *27* (41), 415707.
- (37) Stan, G.; Solares, S. D.; Pittenger, B.; Erina, N.; Su, C. Nanoscale mechanics by tomographic contact resonance atomic force microscopy. *Nanoscale* **2014**, *6* (2), 962–969.
- (38) Killgore, J. P.; Geiss, R. H.; Hurley, D. C. Continuous Measurement of Atomic Force Microscope Tip Wear by Contact Resonance Force Microscopy. *Small* **2011**, *7* (8), 1018–1022.
- (39) Lee, B.; Prater, C. B.; King, W. P. Lorentz force actuation of a heated atomic force microscope cantilever. *Nanotechnology* **2012**, *23* (5), 055709.
- (40) Killgore, J. P.; Tung, R. C.; Hurley, D. C. Characterizing the free and surface-coupled vibrations of heated-tip atomic force microscope cantilevers. *Nanotechnology* **2014**, *25* (34), 345701.
- (41) Ciesielski, P. N.; Resch, M. G.; Hewetson, B.; Killgore, J. P.; Curtin, A.; Anderson, N.; Chiaramonti, A. N.; Hurley, D. C.; Sanders, A.; Himmel, M. E.; Chapple, C.; Mosier, N.; Donohoe, B. S. Engineering plant cell walls: tuning lignin monomer composition for deconstructable biofuel feedstocks or resilient biomaterials. *Green Chem.* **2014**, *16* (5), 2627–2635.

- (42) Nair, S. S.; Wang, S.; Hurley, D. C. Nanoscale characterization of natural fibers and their composites using contact-resonance force microscopy. *Composites, Part A* **2010**, *41* (5), 624–631.
- (43) Wagner, R.; Moon, R. J.; Raman, A. Mechanical properties of cellulose nanomaterials studied by contact resonance atomic force microscopy. *Cellulose* **2016**, *23* (2), 1031–1041.
- (44) Yuya, P. A.; Hurley, D. C.; Turner, J. A. Contact-resonance atomic force microscopy for viscoelasticity. *J. Appl. Phys.* **2008**, *104* (7), 074916.
- (45) Yuya, P. A.; Hurley, D. C.; Turner, J. A. Relationship between Q-factor and sample damping for contact resonance atomic force microscope measurement of viscoelastic properties. *J. Appl. Phys.* **2011**, *109* (11), 113528.
- (46) Campbell, S. E.; Ferguson, V. L.; Hurley, D. C. Nano-mechanical mapping of the osteochondral interface with contact resonance force microscopy and nanoindentation. *Acta Biomater.* **2012**, *8* (12), 4389–4396.
- (47) Hurley, D. C.; Campbell, S. E.; Killgore, J. P.; Cox, L. M.; Ding, Y. Measurement of Viscoelastic Loss Tangent with Contact Resonance Modes of Atomic Force Microscopy. *Macromolecules* **2013**, *46* (23), 9396–9402.
- (48) Putman, C. A. J.; Van der Werf, K. O.; De Grooth, B. G.; Van Hulst, N. F.; Greve, J. Tapping mode atomic force microscopy in liquid. *Appl. Phys. Lett.* **1994**, *64* (18), 2454–2456.
- (49) Schäffer, T. E.; Cleveland, J. P.; Ohnesorge, F.; Walters, D. A.; Hansma, P. K. Studies of vibrating atomic force microscope cantilevers in liquid. *J. Appl. Phys.* **1996**, *80* (7), 3622–3627.
- (50) Han, W.; Lindsay, S. M.; Jing, T. A magnetically driven oscillating probe microscope for operation in liquids. *Appl. Phys. Lett.* **1996**, *69* (26), 4111–4113.
- (51) Revenko, I.; Proksch, R. Magnetic and acoustic tapping mode microscopy of liquid phase phospholipid bilayers and DNA molecules. *J. Appl. Phys.* **2000**, *87* (1), 526–533.
- (52) Ratcliff, G. C.; Erie, D. A.; Superfine, R. Photothermal modulation for oscillating mode atomic force microscopy in solution. *Appl. Phys. Lett.* **1998**, *72* (15), 1911–1913.
- (53) Umeda, N.; Ishizaki, S.; Uwai, H. Scanning attractive force microscope using photothermal vibration. *J. Vac. Sci. Technol., B: Microelectron. Process. Phenom.* **1991**, *9* (2), 1318–1322.
- (54) Gannepalli, A.; Sebastian, A.; Cleveland, J.; Salapaka, M. Thermally driven non-contact atomic force microscopy. *Appl. Phys. Lett.* **2005**, *87* (11), 111901.
- (55) Long, C. J.; Cannara, R. J. Modular apparatus for electrostatic actuation of common atomic force microscope cantilevers. *Rev. Sci. Instrum.* **2015**, *86* (7), 073703.
- (56) Umeda, K.-i.; Kobayashi, K.; Matsushige, K.; Yamada, H. Direct actuation of cantilever in aqueous solutions by electrostatic force using high-frequency electric fields. *Appl. Phys. Lett.* **2012**, *101* (12), 123112.
- (57) Yamanaka, K.; Maruyama, Y.; Tsuji, T.; Nakamoto, K. Resonance frequency and Q factor mapping by ultrasonic atomic force microscopy. *Appl. Phys. Lett.* **2001**, *78* (13), 1939–1941.
- (58) Stan, G.; King, S. W.; Cook, R. F. Nanoscale mapping of contact stiffness and damping by contact resonance atomic force microscopy. *Nanotechnology* **2012**, *23* (21), 215703.
- (59) Rodriguez, B. J.; Callahan, C.; Kalinin, S. V.; Proksch, R. Dual-frequency resonance-tracking atomic force microscopy. *Nanotechnology* **2007**, *18* (47), 475504.
- (60) Kalinin, S. V.; Rodriguez, B. J.; Jesse, S.; Maksymovych, P.; Seal, K.; Nikiforov, M.; Baddorf, A. P.; Kholkin, A. L.; Proksch, R. Local bias-induced phase transitions. *Mater. Today* **2008**, *11* (11), 16–27.
- (61) Gannepalli, A.; Yablon, D. G.; Tsou, A. H.; Proksch, R. Mapping nanoscale elasticity and dissipation using dual frequency contact resonance AFM. *Nanotechnology* **2011**, *22* (35), 355705.
- (62) Jesse, S.; Kalinin, S. V.; Proksch, R.; Baddorf, A. P.; Rodriguez, B. J. The band excitation method in scanning probe microscopy for rapid mapping of energy dissipation on the nanoscale. *Nanotechnology* **2007**, *18* (43), 435503.
- (63) Kos, A. B.; Hurley, D. C. Nanomechanical mapping with resonance tracking scanned probe microscope. *Meas. Sci. Technol.* **2008**, *19* (1), 015504.
- (64) Kos, A. B.; Killgore, J. P.; Hurley, D. C. SPRITE: a modern approach to scanning probe contact resonance imaging. *Meas. Sci. Technol.* **2014**, *25* (2), 025405.
- (65) Pittenger, B.; Yablon, D. Quantitative Measurements of Elastic and Viscoelastic Properties with FASTForce Volume CR, 2017.
- (66) Yablon, D. G.; Gannepalli, A.; Proksch, R.; Killgore, J.; Hurley, D. C.; Grabowski, J.; Tsou, A. H. Quantitative Viscoelastic Mapping of Polyolefin Blends with Contact Resonance Atomic Force Microscopy. *Macromolecules* **2012**, *45* (10), 4363–4370.
- (67) Yablon, D. G.; Grabowski, J.; Chakraborty, I. Measuring the loss tangent of polymer materials with atomic force microscopy based methods. *Meas. Sci. Technol.* **2014**, *25* (5), 055402.
- (68) Rabe, U.; Turner, J.; Arnold, W. Analysis of the high-frequency response of atomic force microscope cantilevers. *Appl. Phys. A: Mater. Sci. Process.* **1998**, *66* (1), S277–S282.
- (69) Hurley, D. C.; Turner, J. A. Humidity effects on the determination of elastic properties by atomic force acoustic microscopy. *J. Appl. Phys.* **2004**, *95* (5), 2403–2407.
- (70) Tung, R. C.; Killgore, J. P.; Hurley, D. C. Hydrodynamic corrections to contact resonance atomic force microscopy measurements of viscoelastic loss tangent. *Rev. Sci. Instrum.* **2013**, *84* (7), 073703.
- (71) Tung, R. C.; Killgore, J. P.; Hurley, D. C. Liquid contact resonance atomic force microscopy via experimental reconstruction of the hydrodynamic function. *J. Appl. Phys.* **2014**, *115* (22), 224904.
- (72) Hurley, D. C. Contact Resonance Force Microscopy Techniques for Nanomechanical Measurements. In *Applied Scanning Probe Methods XI: Scanning Probe Microscopy Techniques*; Springer: Berlin, 2009; pp 97–138.
- (73) Hurley, D. C.; Killgore, J. P. Dynamic Contact AFM Methods for Nanomechanical Properties. In *Scanning Probe Microscopy in Industrial Applications*; John Wiley & Sons, Inc.: Hoboken, NJ, 2013.
- (74) Rabe, U. Atomic Force Acoustic Microscopy. In *Applied Scanning Probe Methods II: Scanning Probe Microscopy Techniques*, Bhushan, B.; Fuchs, H., Eds.; Springer: Berlin, 2006; pp 37–90.
- (75) Kolosov, O.; Yamanaka, K. Nonlinear Detection of Ultrasonic Vibrations in an Atomic Force Microscope. *Jpn. J. Appl. Phys.* **1993**, *32* (8A), L1095.
- (76) Meyer, G.; Amer, N. M. Erratum: Novel optical approach to atomic force microscopy [Appl. Phys. Lett. 53, 1045 (1988)]. *Appl. Phys. Lett.* **1988**, *53* (24), 2400–2402.
- (77) Binnig, G.; Quate, C. F.; Gerber, C. Atomic Force Microscope. *Phys. Rev. Lett.* **1986**, *56* (9), 930–933.
- (78) Zhong, Q.; Inniss, D.; Kjoller, K.; Elings, V. B. Fractured polymer/silica fiber surface studied by tapping mode atomic force microscopy. *Surf. Sci.* **1993**, *290* (1-2), L688–L692.
- (79) Florin, E. L.; Radmacher, M.; Fleck, B.; Gaub, H. E. Atomic force microscope with magnetic force modulation. *Rev. Sci. Instrum.* **1994**, *65* (3), 639–643.
- (80) Hansma, P. K.; Cleveland, J. P.; Radmacher, M.; Walters, D. A.; Hillner, P. E.; Bezanilla, M.; Fritz, M.; Vie, D.; Hansma, H. G.; Prater, C. B.; Massie, J.; Fukunaga, L.; Gurley, J.; Elings, V. Tapping mode atomic force microscopy in liquids. *Appl. Phys. Lett.* **1994**, *64* (13), 1738–1740.
- (81) Weisenhorn, A. L.; Hansma, P. K.; Albrecht, T. R.; Quate, C. F. Forces in atomic force microscopy in air and water. *Appl. Phys. Lett.* **1989**, *54* (26), 2651–2653.
- (82) Rabe, U.; Janser, K.; Arnold, W. Vibrations of free and surface-coupled atomic force microscope cantilevers: Theory and experiment. *Rev. Sci. Instrum.* **1996**, *67* (9), 3281–3293.
- (83) Turner, J. A.; Hirsekorn, S.; Rabe, U.; Arnold, W. High-frequency response of atomic-force microscope cantilevers. *J. Appl. Phys.* **1997**, *82* (3), 966–979.
- (84) Yamanaka, K.; Noguchi, A.; Tsuji, T.; Koike, T.; Goto, T. Quantitative material characterization by ultrasonic AFM. *Surf. Interface Anal.* **1999**, *27* (5–6), 600–606.

- (85) Wright, O. B.; Nishiguchi, N. Vibrational dynamics of force microscopy: Effect of tip dimensions. *Appl. Phys. Lett.* **1997**, *71* (5), 626–628.
- (86) Mazeran, P.-E.; Loubet, J.-L. Force modulation with a scanning force microscope: an analysis. *Tribol. Lett.* **1997**, *3* (1), 125–132.
- (87) Hurley, D. C.; Shen, K.; Jennett, N. M.; Turner, J. A. Atomic force acoustic microscopy methods to determine thin-film elastic properties. *J. Appl. Phys.* **2003**, *94* (4), 2347–2354.
- (88) Dupas, E.; Gremaud, G.; Kulik, A.; Loubet, J.-L. High-frequency mechanical spectroscopy with an atomic force microscope. *Rev. Sci. Instrum.* **2001**, *72* (10), 3891–3897.
- (89) Dokukin, M. E.; Sokolov, I. On the Measurements of Rigidity Modulus of Soft Materials in Nanoindentation Experiments at Small Depth. *Macromolecules* **2012**, *45* (10), 4277–4288.
- (90) Hertz, H. Über die Berührung fester elastischer Körper. *J. reine und angewandte Mathematik* **1882**, *92*, 156–171.
- (91) Rabe, U.; Amelio, S.; Kopycynska, M.; Hirsekorn, S.; Kempf, M.; Göken, M.; Arnold, W. Imaging and measurement of local mechanical material properties by atomic force acoustic microscopy. *Surf. Interface Anal.* **2002**, *33* (2), 65–70.
- (92) Briscoe, B. J.; Fiori, L.; Pelillo, E. Nano-indentation of polymeric surfaces. *J. Phys. D: Appl. Phys.* **1998**, *31* (19), 2395.
- (93) Tweedie, C. A.; Constantinides, G.; Lehman, K. E.; Brill, D. J.; Blackman, G. S.; VanVliet, K. J. Enhanced Stiffness of Amorphous Polymer Surfaces under Confinement of Localized Contact Loads. *Adv. Mater.* **2007**, *19* (18), 2540–2546.
- (94) Zhou, J.; Komvopoulos, K. Interfacial viscoelasticity of thin polymer films studied by nanoscale dynamic mechanical analysis. *Appl. Phys. Lett.* **2007**, *90* (2), 021910.
- (95) Dimitriadis, E. K.; Horkay, F.; Maresca, J.; Kachar, B.; Chadwick, R. S. Determination of Elastic Moduli of Thin Layers of Soft Material Using the Atomic Force Microscope. *Biophys. J.* **2002**, *82* (5), 2798–2810.
- (96) Loubet, J. L.; Oliver, W. C.; Lucas, B. N. Measurement of the loss tangent of low-density polyethylene with a nanoindentation technique. *J. Mater. Res.* **2000**, *15* (5), 1195–1198.
- (97) Asif, S. A. S.; Wahl, K. J.; Colton, R. J.; Warren, O. L. Quantitative imaging of nanoscale mechanical properties using hybrid nanoindentation and force modulation. *J. Appl. Phys.* **2001**, *90* (3), 1192–1200.
- (98) Araki, O.; Shimamoto, T.; Yamamoto, T.; Masuda, T. Physical aging of polystyrene investigated by dynamic viscoelasticity. *Polymer* **2001**, *42* (9), 4433–4437.
- (99) Joshi, M.; Butola, B. S.; Simon, G.; Kukaleva, N. Rheological and Viscoelastic Behavior of HDPE/Octamethyl-POSS Nanocomposites. *Macromolecules* **2006**, *39* (5), 1839–1849.
- (100) Monclus, M. A.; Jennett, N. M. In search of validated measurements of the properties of viscoelastic materials by indentation with sharp indenters. *Philos. Mag.* **2011**, *91* (7–9), 1308–1328.
- (101) Ferry, J. D. *Viscoelastic Properties of Polymers*; John Wiley & Sons: New York, 1980.
- (102) Caron, A.; Arnold, W. Observation of local internal friction and plasticity onset in nanocrystalline nickel by atomic force acoustic microscopy. *Acta Mater.* **2009**, *57* (15), 4353–4363.
- (103) Wagner, H.; Büchsenstütz-Göbeler, M.; Luo, Y.; Kumar, A.; Arnold, W.; Samwer, K. Measurement of local internal friction in metallic glasses. *J. Appl. Phys.* **2014**, *115* (13), 134307.
- (104) Stan, G.; King, S. W.; Cook, R. F. Elastic modulus of low-k dielectric thin films measured by load-dependent contact-resonance atomic force microscopy. *J. Mater. Res.* **2009**, *24* (9), 2960–2964.
- (105) Proksch, R.; Babcock, K.; Cleveland, J. Magnetic dissipation microscopy in ambient conditions. *Appl. Phys. Lett.* **1999**, *74* (3), 419–421.
- (106) Killgore, J. P.; Yablon, D. G.; Tsou, A. H.; Gannepalli, A.; Yuya, P. A.; Turner, J. A.; Proksch, R.; Hurley, D. C. Viscoelastic Property Mapping with Contact Resonance Force Microscopy. *Langmuir* **2011**, *27* (23), 13983–13987.
- (107) Yamashita, J.; Li, X.; Furman, B. R.; Rawls, H. R.; Wang, X.; Agrawal, C. M. Collagen and bone viscoelasticity: A dynamic mechanical analysis. *J. Biomed. Mater. Res.* **2002**, *63* (1), 31–36.
- (108) Fulcher, G. R.; Hukins, D. W.; Shepherd, D. E. Viscoelastic properties of bovine articular cartilage attached to subchondral bone at high frequencies. *BMC Musculoskeletal Disord.* **2009**, *10* (1), 61.
- (109) Proksch, R.; Yablon, D. G. Loss tangent imaging: Theory and simulations of repulsive-mode tapping atomic force microscopy. *Appl. Phys. Lett.* **2012**, *100* (7), 073106.
- (110) Cappella, B.; Kaliappan, S. K.; Sturm, H. Using AFM Force–Distance Curves To Study the Glass-to-Rubber Transition of Amorphous Polymers and Their Elastic–Plastic Properties as a Function of Temperature. *Macromolecules* **2005**, *38* (5), 1874–1881.
- (111) Fasolka, M. J.; Mayes, A. M.; Magonov, S. N. Thermal enhancement of AFM phase contrast for imaging diblock copolymer thin film morphology. *Ultramicroscopy* **2001**, *90* (1), 21–31.
- (112) Kajiyama, T.; Tanaka, K.; Takahara, A. Surface molecular motion of the monodisperse polystyrene films. *Macromolecules* **1997**, *30* (2), 280–285.
- (113) Ge, S.; Pu, Y.; Zhang, W.; Rafailovich, M.; Sokolov, J.; Buenviaje, C.; Buckmaster, R.; Overney, R. M. Shear Modulation Force Microscopy Study of Near Surface Glass Transition Temperatures. *Phys. Rev. Lett.* **2000**, *85* (11), 2340–2343.
- (114) Menczel, J. D.; Prime, R. B. *Thermal Analysis of Polymers: Fundamentals and Applications*; John Wiley & Sons: 2014.
- (115) Jesse, S.; Nikiforov, M. P.; Germinario, L. T.; Kalinin, S. V. Local thermomechanical characterization of phase transitions using band excitation atomic force acoustic microscopy with heated probe. *Appl. Phys. Lett.* **2008**, *93* (7), 073104.
- (116) Nikiforov, M. P.; Jesse, S.; Morozovska, A. N.; Eliseev, E. A.; Germinario, L. T.; Kalinin, S. V. Probing the temperature dependence of the mechanical properties of polymers at the nanoscale with band excitation thermal scanning probe microscopy. *Nanotechnology* **2009**, *20* (39), 395709.
- (117) Chakraborty, I.; Yablon, D. G. Temperature dependent loss tangent measurement of polymers with contact resonance atomic force microscopy. *Polymer* **2014**, *55* (7), 1609–1612.
- (118) Natali, M.; Passeri, D.; Reggente, M.; Tamburri, E.; Terranova, M. L.; Rossi, M. Contact resonance atomic force microscopy for viscoelastic characterization of polymer-based nanocomposites at variable temperature. *AIP Conf. Proc.* **2015**, *1749* (1), 020008.
- (119) Parlak, Z.; Tu, Q.; Zauscher, S. Liquid contact resonance AFM: analytical models, experiments, and limitations. *Nanotechnology* **2014**, *25* (44), 445703.
- (120) Kocun, M.; Labuda, A.; Gannepalli, A.; Proksch, R. Contact resonance atomic force microscopy imaging in air and water using photothermal excitation. *Rev. Sci. Instrum.* **2015**, *86* (8), 083706.
- (121) DelRio, F. W.; Jaye, C.; Fischer, D. A.; Cook, R. F. Elastic and adhesive properties of alkanethiol self-assembled monolayers on gold. *Appl. Phys. Lett.* **2009**, *94* (13), 131909.
- (122) DelRio, F. W.; Steffens, K. L.; Jaye, C.; Fischer, D. A.; Cook, R. F. Elastic, Adhesive, and Charge Transport Properties of a Metal–Molecule–Metal Junction: The Role of Molecular Orientation, Order, and Coverage. *Langmuir* **2010**, *26* (3), 1688–1699.
- (123) DelRio, F. W.; Rampulla, D. M.; Jaye, C.; Stan, G.; Gates, R. S.; Fischer, D. A.; Cook, R. F. Structure–property relationships for methyl-terminated alkyl self-assembled monolayers. *Chem. Phys. Lett.* **2011**, *512* (4), 243–246.
- (124) Mirman, B.; Kalinin, S. V. Resonance frequency analysis for surface-coupled atomic force microscopy cantilever in ambient and liquid environments. *Appl. Phys. Lett.* **2008**, *92* (8), 083102.
- (125) Farokh Payam, A. Sensitivity of flexural vibration mode of the rectangular atomic force microscope micro cantilevers in liquid to the surface stiffness variations. *Ultramicroscopy* **2013**, *135*, 84–88.
- (126) Ploscaru, N.; Szoszkiewicz, R. A method to measure nanomechanical properties of biological objects. *Appl. Phys. Lett.* **2013**, *103* (26), 263702.

- (127) Churnside, A. B.; Tung, R. C.; Killgore, J. P. Quantitative Contact Resonance Force Microscopy for Viscoelastic Measurement of Soft Materials at the Solid–Liquid Interface. *Langmuir* **2015**, *31* (40), 11143–11149.
- (128) Rupp, D.; Rabe, U.; Hirsekorn, S.; Arnold, W. Nonlinear contact resonance spectroscopy in atomic force microscopy. *J. Phys. D: Appl. Phys.* **2007**, *40* (22), 7136.
- (129) Glover, C. C.; Killgore, J. P.; Tung, R. C. Scanning speed phenomenon in contact-resonance atomic force microscopy. *Beilstein J. Nanotechnol.* **2018**, *9*, 945–952.
- (130) Wagner, R.; Killgore, J. P.; Tung, R. C.; Raman, A.; Hurley, D. C. Vibrational shape tracking of atomic force microscopy cantilevers for improved sensitivity and accuracy of nanomechanical measurements. *Nanotechnology* **2015**, *26* (4), 045701.
- (131) Radmacher, M.; Tillmann, R. W.; Gaub, H. E. Imaging viscoelasticity by force modulation with the atomic force microscope. *Biophys. J.* **1993**, *64* (3), 735–742.
- (132) Yang, N.; Wong, K. K. H.; de Bruyn, J. R.; Hutter, J. L. Frequency-dependent viscoelasticity measurement by atomic force microscopy. *Meas. Sci. Technol.* **2009**, *20* (2), 025703.
- (133) Wagner, R.; Killgore, J. P. Photothermally excited force modulation microscopy for broadband nanomechanical property measurements. *Appl. Phys. Lett.* **2015**, *107* (20), 203111.
- (134) Yuya, P. A.; Patel, N. G. Analytical model for nanoscale viscoelastic properties characterization using dynamic nanoindentation. *Philos. Mag.* **2014**, *94* (22), 2505–2519.
- (135) Killgore, J. P.; Hurley, D. C. Pulsed contact resonance for atomic force microscopy nanomechanical measurements. *Appl. Phys. Lett.* **2012**, *100* (5), 053104.
- (136) Stan, G.; Gates, R. S. Intermittent contact resonance atomic force microscopy. *Nanotechnology* **2014**, *25* (24), 245702.
- (137) Parlak, Z.; Degertekin, F. L. Combined quantitative ultrasonic and time-resolved interaction force AFM imaging. *Rev. Sci. Instrum.* **2011**, *82* (1), 013703.
- (138) George, J.; Sreekala, M. S.; Thomas, S. A review on interface modification and characterization of natural fiber reinforced plastic composites. *Polym. Eng. Sci.* **2001**, *41* (9), 1471–1485.
- (139) Coleman, J. N.; Khan, U.; Blau, W. J.; Gun'ko, Y. K. Small but strong: A review of the mechanical properties of carbon nanotube–polymer composites. *Carbon* **2006**, *44* (9), 1624–1652.
- (140) Frazier, W. E. Metal Additive Manufacturing: A Review. *J. Mater. Eng. Perform.* **2014**, *23* (6), 1917–1928.
- (141) Ligon, S. C.; Liska, R.; Stampfl, J.; Gurr, M.; Mühlaupt, R. Polymers for 3D Printing and Customized Additive Manufacturing. *Chem. Rev.* **2017**, *117* (15), 10212–10290.
- (142) Kim, H.-C.; Park, S.-M.; Hinsberg, W. D. Block Copolymer Based Nanostructures: Materials, Processes, and Applications to Electronics. *Chem. Rev.* **2010**, *110* (1), 146–177.
- (143) Mai, Y.; Eisenberg, A. Self-assembly of block copolymers. *Chem. Soc. Rev.* **2012**, *41* (18), 5969–5985.
- (144) Elsbahy, M.; Heo, G. S.; Lim, S.-M.; Sun, G.; Wooley, K. L. Polymeric Nanostructures for Imaging and Therapy. *Chem. Rev.* **2015**, *115* (19), 10967–11011.
- (145) Tatum, W. K.; Luscombe, C. K. π -Conjugated polymer nanowires: advances and perspectives toward effective commercial implementation. *Polym. J.* **2018**, *50*, 659.
- (146) Tsai, D.-H.; DelRio, F. W.; Keene, A. M.; Tyner, K. M.; MacCuspie, R. I.; Cho, T. J.; Zachariah, M. R.; Hackley, V. A. Adsorption and Conformation of Serum Albumin Protein on Gold Nanoparticles Investigated Using Dimensional Measurements and in Situ Spectroscopic Methods. *Langmuir* **2011**, *27* (6), 2464–2477.
- (147) Tsai, D.-H.; Elzey, S.; DelRio, F. W.; Keene, A. M.; Tyner, K. M.; Clogston, J. D.; MacCuspie, R. I.; Guha, S.; Zachariah, M. R.; Hackley, V. A. Tumor necrosis factor interaction with gold nanoparticles. *Nanoscale* **2012**, *4* (10), 3208–3217.
- (148) Tsai, D.-H.; Cho, T. J.; DelRio, F. W.; Gorham, J. M.; Zheng, J.; Tan, J.; Zachariah, M. R.; Hackley, V. A. Controlled Formation and Characterization of Dithiothreitol-Conjugated Gold Nanoparticle Clusters. *Langmuir* **2014**, *30* (12), 3397–3405.
- (149) Yang, C.; DelRio, F. W.; Ma, H.; Killaars, A. R.; Basta, L. P.; Kyburz, K. A.; Anseth, K. S. Spatially patterned matrix elasticity directs stem cell fate. *Proc. Natl. Acad. Sci. U. S. A.* **2016**, *113* (31), E4439–E4445.
- (150) Rosales, A. M.; Vega, S. L.; DelRio, F. W.; Burdick, J. A.; Anseth, K. S. Hydrogels with Reversible Mechanics to Probe Dynamic Cell Microenvironments. *Angew. Chem.* **2017**, *129* (40), 12300–12304.
- (151) Wahlquist, J. A.; DelRio, F. W.; Randolph, M. A.; Aziz, A. H.; Heveran, C. M.; Bryant, S. J.; Neu, C. P.; Ferguson, V. L. Indentation mapping revealed poroelastic, but not viscoelastic, properties spanning native zonal articular cartilage. *Acta Biomater.* **2017**, *64*, 41–49.

Correction to Contact Resonance Force Microscopy for Viscoelastic Property Measurements: From Fundamentals to State-of-the-Art Applications

Jason P. Killgore* and Frank W. DelRio*¹

Macromolecules 2018, 51 (18), 6977–6996. DOI: 10.1021/acs.macromol.8b01178

In the original paper,¹ the authors erroneously took the wrong figure from the cited paper² to generate Figure 8a. The figure was intended to compare acoustic excitation to magnetic excitation in liquid and illustrate that magnetic excitation resulted in a more Lorentzian peak shape with a well-defined frequency and quality factor that shifted when the tip–sample contact stiffness was varied (as opposed to the original version, which mistakenly showed acoustic excitation data for both the first and second eigenmodes). The new figure and caption for Figure 8 are shown below.

REFERENCES

- (1) Killgore, J. P.; DelRio, F. W. Contact Resonance Force Microscopy for Viscoelastic Property Measurements: From Fundamentals to State-of-the-Art Applications. *Macromolecules* 2018, 51 (18), 6977–6996.
- (2) Parlak, Z.; Tu, Q.; Zauscher, S. Liquid contact resonance AFM: analytical models, experiments, and limitations. *Nanotechnology* 2014, 25 (44), 445703.

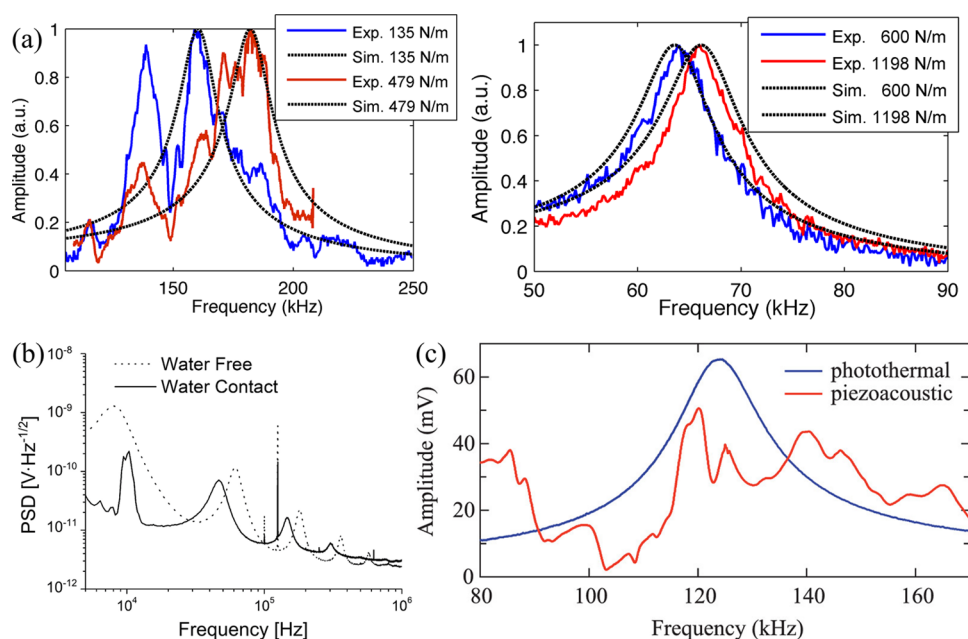


Figure 8. Cantilever excitation methods for viscoelastic CRFM in liquid environments. (a) Experimental and simulated contact resonance frequency spectra for a cantilever actuated via piezoacoustic (left) and magnetic (right) excitation (first eigenmode). The magnetically driven excitation was achieved via a neodymium particle adhered to the backside of the cantilever and driven by a solenoid. Reproduced with permission from ref 119. Copyright 2014 IOP Publishing. (b) Experimental free and contact frequency spectra for a cantilever actuated via the Brownian motion of the surrounding fluid. The peaks at 100 and 125 kHz are artifacts of the instrument controller, whereas the peaks at 10 kHz are noise. Reproduced with permission from ref 71. Copyright 2014 American Institute of Physics. (c) Experimental contact resonance frequency spectra for a cantilever actuated via piezoacoustic and photothermal excitation; the piezoacoustic signal exhibited multiple peaks, while the photothermal signal showed a clean peak at 124.1 kHz with a quality factor of 8.1. Reproduced with permission from ref 120. Copyright 2015 American Institute of Physics.

Published: October 5, 2018

